



An asymptotic-preserving conservative semi-Lagrangian scheme for the Vlasov-Maxwell system in the quasi-neutral limit

Hongtao Liu^a, Xiaofeng Cai^{b,c,*}, Yong Cao^{d,*}, Giovanni Lapenta^a

^a Center for Mathematical Plasma Astrophysics, Department of Mathematics, KU Leuven, Leuven, 3001, Belgium

^b Research Center of Mathematics, Advanced Institute of Natural Sciences, Beijing Normal University, Zhuhai, 519087, China

^c Guangdong Provincial Key Laboratory of Interdisciplinary Research and Application for Data Science, BNU-HKBU United International College, Zhuhai, 519087, China

^d School of Mechanical Engineering and Automation, Harbin Institute of Technology, Shenzhen, 518055, China

ARTICLE INFO

Keywords:

Plasma physics
Vlasov-Maxwell system
Semi-Lagrangian scheme
Quasi-neutral limit
Asymptotic preserving scheme

ABSTRACT

In this paper, we present an asymptotic-preserving conservative Semi-Lagrangian (CSL) scheme for the Vlasov-Maxwell system in the quasi-neutral limit, where the Debye length is negligible compared to the macroscopic scales of interest. The proposed method relies on two key ingredients: the CSL scheme and a reformulated Maxwell equation (RME). The CSL scheme is employed for the phase space discretization of the Vlasov equation, ensuring mass conservation and removing the Courant-Friedrichs-Lewy restriction, thereby enhancing computational efficiency. To efficiently calculate the electromagnetic field in both non-neutral and quasi-neutral regimes, the RME is derived by semi-implicitly coupling the Maxwell equation and the moments of the Vlasov equation. Furthermore, we apply Gauss's law correction to the electric field derived from the RME to prevent unphysical charge separation. The synergy of the CSL and RME enables the proposed method to provide reliable solutions, even when the spatial and temporal resolution might not fully resolve the Debye length and plasma period. As a result, the proposed method offers a unified and accurate numerical simulation approach for complex electromagnetic plasma physics while maintaining efficiency in both quasi-neutral and non-quasi-neutral regimes. Several numerical experiments, ranging from 3D to 5D simulations, are presented to demonstrate the accuracy, stability, and efficiency of the proposed method.

1. Introduction

Electromagnetic plasma finds applications in various fields such as space propulsion, material processing, space physics, astrophysical physics, and confined fusion devices [1]. However, accurately simulating plasma dynamics numerically poses significant challenges due to the diverse range of physical scenarios involved. To describe plasma dynamics, two major models are commonly used: fluid models, which focus on macroscopic quantities in physical space, and kinetic models, which consider microscopic distri-

* Corresponding authors.

E-mail addresses: hongtao.liu@kuleuven.be (H. Liu), xfcai@bnu.edu.cn (X. Cai), yongc@hit.edu.cn (Y. Cao), giovanni.lapenta@kuleuven.be (G. Lapenta).

<https://doi.org/10.1016/j.jcp.2025.113840>

Received 10 June 2024; Received in revised form 5 December 2024; Accepted 9 February 2025

bution functions in phase space. While fluid models are generally efficient, they may not adequately capture local kinetic scales [2]. Given the complex multi-scale nature of many plasma phenomena, a kinetic model is desired when aiming for a unified and accurate method capable of addressing cross-scales.

One basic kinetic model for electromagnetic plasma simulations is the Vlasov-Maxwell (VM) system. A critical parameter in this model is the normalized Debye length λ , which represents the ratio of the Debye length to the macroscopic scales of interest. It indicates the strength of Debye shielding and charge separation effects. When $\lambda \rightarrow 0$, the VM system enters the quasi-neutral limit, where charge separations can be neglected. On the other hand, when $\lambda \sim O(1)$, the system transitions into the non-quasi-neutral regime, requiring the consideration of charge separation effects. When both quasi-neutral and non-quasi-neutral regimes coexist, neither quasi-neutral models nor non-neutral models are appropriate to describe the multi-scale transitions [3], posing a significant challenge for numerically simulating the complex electromagnetic plasma physics. Furthermore, traditional explicit schemes require numerical grid spacing and time step sizes that should resolve the microscopic normalized Debye length λ while conducting simulations on a macroscopic scale, which is time-consuming. In this paper, our aim is to propose an asymptotic-preserving VM solver that preserves accuracy and efficiency in both the quasi-neutral and the non-quasi-neutral regimes.

Several methods have been proposed for VM system, broadly falling into two categories: particle-based methods and grid-based methods. One well-known particle-based approach is the Particle-In-Cell (PIC) method, which traces the motion of macro-particles [4]. Although PIC is computationally efficient [2,5,6], it suffers from numerical noise, particularly when dealing with small perturbed plasma flows [7,8]. Alternatively, the grid-based methods directly solve the kinetic equation in phase space [9–15] and are referred to as the direct kinetic method (DKM) [16,17]. The DKM is free from numerical noise and enables high-order accuracy for phase space discretization. Various efficient and accurate DKM solvers have been proposed, including Eulerian or semi-Lagrangian finite difference [18–20], finite element [21–23], finite volume [24–27], and spectral methods [7,28]; detailed reviews of these methods can be found in [29–31]. Among these DKM solvers, we focus on the conservative semi-Lagrangian (CSL) scheme, which eliminates the need for the Courant-Friedrichs-Lewy (CFL) condition and ensures mass conservation [32–37]. However, it is important to note that most of these methods were primarily developed for non-quasi-neutral plasma flows.

For problems that involve both quasi-neutral and non-quasi-neutral regimes simultaneously, traditional methods require resolving all scales to ensure stability and consistency, even when certain scales may not be critical. However, directly resolving the smallest scale throughout the entire domain is practically prohibitive. To address this challenge, one numerical strategy is the hybrid method [38,39]. This method divides the computation domain into subdomains with different governing equations corresponding to specific flow regimes. However, establishing an appropriate criterion to couple different methods requires specific treatments, and identifying the dynamic interface between subdomains is not a trivial task.

Alternatively, a promising multiscale method, known as the Asymptotic-Preserving (AP) scheme [40,41], has been proposed to provide a unified approach without the limitation of characteristic parameters on the numerical ones, thereby avoiding the challenges of the hybrid method. A key advantage of AP schemes is their automatic alignment with the discretization of corresponding limiting models when characteristic parameters tend to zero. In the field of plasma physics, several AP schemes have been developed, including the Vlasov-Poisson [42–45], BGK-Vlasov-Poisson [27,46], and VM models [3,47]. Notably, the work of [3] presents a significant advancement by reformulating the Maxwell equation into the reformulated Maxwell equation (RME). This formulation bridges the gap between non-neutral and quasi-neutral regimes, creating a unified framework through the use of a generalized Ohm's law. Consequently, a smooth transition between cross-regimes becomes achievable. Inspired by [3], this study couples the Vlasov equation with the RME, but a conservative semi-Lagrangian solver is utilized instead of the PIC solver as done in [3]. Remarkably, to the best of our knowledge, no AP semi-Lagrangian scheme has been proposed for the VM system in the quasi-neutral limit yet.

The main contribution of this paper is the development of an AP conservative semi-Lagrangian scheme for the VM system, which is based on two key components: the CSL scheme and the RME. Specifically, the CSL scheme is utilized for the phase space discretization of the Vlasov equation, allowing the method to remove the CFL restriction and preserve system mass. The RME provides a straightforward and efficient approach for investigating the electromagnetic field in both quasi-neutral and non-quasi-neutral regimes, by semi-implicitly coupling macroscopic moments of the Vlasov equations and electromagnetic field equations. Additionally, the electric field obtained from the RME is enforced with Gauss's law correction to avoid unphysical charge separation. The combination of the RME and the CSL scheme enables the proposed method to overcome numerical constraints arising from the normalized Debye length. Importantly, the proposed method achieves a comparable numerical cost per time step to explicit schemes without requiring nonlinear iteration. Moreover, the method can be extended to multidimensional plasma simulations using dimensional splitting procedures, further enhancing its efficiency. Finally, several numerical experiments are presented to demonstrate the accuracy, stability, and efficiency of the proposed method for the VM system.

The paper is organized as follows. Section 2 introduces the Vlasov-Maxwell system and its reformulated form. In Section 3, we describe the details of the asymptotic-preserving conservative semi-Lagrangian scheme. The analysis of the method's properties is presented in Section 4. Section 5 presents the results of numerical studies. Finally, a summary is provided in Section 6.

2. The Vlasov-Maxwell system and its reformulated form

In this section, we provide a comprehensive overview of the Vlasov-Maxwell (VM) system and its reformulated form. We begin by introducing the original VM system and its nondimensionalization. Recognizing the challenge posed by the degeneracy in the quasi-neutral limit in the VM system, we present the reformulated VM system, where reformulated Maxwell equations (RME) are formed by the coupling of the macroscopic moments of the Vlasov equation and Maxwell equations.

2.1. The Vlasov-Maxwell system

In this paper, our focus lies on the nonrelativistic VM system, which describes the dynamics of the fully ionized plasma. The evolution of electrons and ions follows the Vlasov equation,

$$\partial_t f_s + \mathbf{v}_s \cdot \nabla_{\mathbf{x}} f_s + \frac{q_s}{m_s} (\mathbf{E} + \mathbf{v}_s \times \mathbf{B}) \cdot \nabla_{\mathbf{v}_s} f_s = 0, \quad (1)$$

where $f_s(\mathbf{x}, \mathbf{v}_s, t)$ represents the distribution function for species s at position \mathbf{x} in physics space, with velocity \mathbf{v}_s at time t . Besides, q_s and m_s denote the charge and mass of species s , respectively, while \mathbf{E} and \mathbf{B} correspond to the electric and magnetic fields. In the current paper, we consider the species s to represent either a single-charged ion ($s = i$) or an electron ($s = e$). However, it is worth noting that the framework and methodology presented in the following sections can be generalized to accommodate arbitrary species.

It is well-established that the self-consistent fields \mathbf{E} and \mathbf{B} can be determined from the Maxwell equations,

$$\begin{aligned} \partial_t \mathbf{E} - c^2 \nabla \times \mathbf{B} &= -c^2 \mu_0 \mathbf{J}, \\ \partial_t \mathbf{B} + \nabla \times \mathbf{E} &= 0, \end{aligned} \quad (2)$$

where c represents the speed of light, μ_0 denotes the vacuum permeability, and \mathbf{J} represents the total current density. Additionally, the electromagnetic fields are subject to two constraints known as Gauss's law and the Thomson-Maxwell equation,

$$\nabla \cdot \mathbf{E} = \rho / \epsilon_0, \quad \nabla \cdot \mathbf{B} = 0, \quad (3)$$

where ϵ_0 is the vacuum permittivity and ρ is the charge density. It is worth noting that these two constraints are valid for $t > 0$ as long as they are satisfied at $t = 0$. However, when considering numerical approximations, these constraints may not always hold true. To address this issue, several corrections [48–50] have been proposed to enforce the constraints. In this paper, we employ elliptic correction of the electric field [3,51] to enforce Gauss's law, and detailed information will be presented in Section 3.3. Besides, the well-known Debye length, denoted as λ_D , and the electron plasma frequency, represented by ω_p , are defined as follows,

$$\lambda_D = \left(\frac{\epsilon k_B T}{q^2 n} \right)^{1/2}, \quad \omega_p = \left(\frac{n q^2}{\epsilon_0 m_e} \right)^{1/2},$$

where k_B is the Boltzmann constant, q is elementary charge, n is number density, and T is temperature.

To facilitate a better understanding of the quasi-neutral limit in the VM system, we introduce the following dimensionless variables [16],

$$\begin{aligned} \bar{x} &= \frac{x}{x_0}, \bar{T} = \frac{T}{T_0}, \bar{m} = \frac{m}{m_0}, \bar{n} = \frac{n}{n_0}, \bar{v} = \frac{v}{v_0}, \\ \bar{t} &= \frac{t}{t_0}, \bar{f} = \frac{f}{f_0}, \bar{\mathbf{J}} = \frac{\mathbf{J}}{J_0}, \bar{\mathbf{E}} = \frac{\mathbf{E}}{E_0}, \bar{\mathbf{B}} = \frac{\mathbf{B}}{B_0}, \end{aligned} \quad (4)$$

where x_0, T_0, m_0, n_0 , are reference length, temperature, mass, and number density. By setting the reference velocity as $v_0 = \sqrt{k_B T_0 / m_0}$ and the magnetic field as $B_0 = m_0 v_0 / q x_0$, we can derive the reference time as $t_0 = x_0 / v_0$, the distribution function as $f_0 = n_0 / v_0^{d_v}$, the total current density as $J_0 = q n_0 v_0$, and the electric field as $E_0 = B_0 v_0$. Once the four parameters x_0, T_0, m_0 , and n_0 are specified, the dimensionless VM system is uniquely determined.

In current study, we chose $T_0 = T_e, m_0 = m_e, n_0 = n_e$, unless specifically stated otherwise. The reference length x_0 will be given in the specific simulation. The dimensionless Debye length is defined as $\lambda = \lambda_D / x_0$. In the rest of paper, all variables are dimensionless unless stated otherwise, but we will drop the bar over the variables for simplicity. Then the dimensionless VM system Eqs. (1) and (2) can be written as

$$\partial_t f_s + \mathbf{v}_s \cdot \nabla_{\mathbf{x}} f_s + \frac{q_s}{m_s} (\mathbf{E} + \mathbf{v}_s \times \mathbf{B}) \cdot \nabla_{\mathbf{v}_s} f_s = 0, \quad (5)$$

$$\lambda^2 \partial_t \mathbf{E} - \lambda^2 c^2 \nabla \times \mathbf{B} = -\mathbf{J}, \quad (6)$$

$$\partial_t \mathbf{B} + \nabla \times \mathbf{E} = 0. \quad (7)$$

Once the distribution function f_s is known, the conservative variables \mathbf{W}_s for species s can be obtained by

$$\mathbf{W}_s = (n_s, n_s \mathbf{u}_s, E_{k_s})^T = \int_{\Omega_v} \boldsymbol{\psi} f_s d\mathbf{v}, \quad (8)$$

where Ω_v represents the velocity domain, $\boldsymbol{\psi} = (1, \mathbf{v}_s, \mathbf{v}_s^2 / 2)^T$ is the collision invariant, \mathbf{u}_s is the plasma velocity, and E_{k_s} is the kinetic energy. Then the charge density ρ_s and current density \mathbf{J}_s for species s can be obtained from

$$(\rho_s, \mathbf{J}_s)^T = q_s (n_s, n_s \mathbf{u}_s)^T. \quad (9)$$

The total charge density ρ and current density \mathbf{J} can be further given by

$$(\rho, \mathbf{J})^T = \sum_s (\rho_s, \mathbf{J}_s)^T.$$

2.2. The reformulated Vlasov Maxwell system

It is worth noting that in the quasi-neutral limit as $\lambda \rightarrow 0$, the VM system (5), (6), and (7) cannot be directly used for numerical approximation, since the electric field \mathbf{E} could not be directly obtained from Ampère law (6). Specifically, in this limit, the displacement current vanishes, and electromagnetic waves propagate at velocities much smaller than the speed of light [3], with $c \rightarrow 1/\lambda$. As a result, Eq. (6) simplifies to $\mathbf{J} = \nabla \times \mathbf{B}$, which implies $\nabla \cdot \mathbf{J} = 0$. To address the degeneracy of the quasi-neutral limit, Degond et al. [3] proposed the reformulated VM system, which will be briefly introduced as follows.

Taking the first moment of the Vlasov equation (5) and multiplying the momentum equation by q_s , we obtain the following relation for the current density, which can be viewed as a generalized Ohm's law [52],

$$\partial_t \mathbf{J} = \bar{\rho} \mathbf{E} + \bar{\mathbf{J}} \times \mathbf{B} - \nabla \cdot \bar{\mathbf{P}}, \quad (11)$$

where $(\bar{\rho}, \bar{\mathbf{J}})^T = \frac{q_s}{m_s} \sum_s (\rho_s, \mathbf{J}_s)^T$ and $\bar{\mathbf{P}} = q_s \sum_s \int \mathbf{v} \mathbf{v} f_s d\mathbf{v}_s$. By combining Eq. (6) with the generalized Ohm's law Eq. (11), we can derive the RME,

$$\lambda^2 \partial_t^2 \mathbf{E} + \bar{\rho} \mathbf{E} + \lambda^2 c^2 \nabla \times \nabla \times \mathbf{E} = \nabla \cdot \bar{\mathbf{P}} - \bar{\mathbf{J}} \times \mathbf{B}. \quad (12)$$

Consequently, the reformulated VM system is defined as follows,

$$\partial_t f_s + \mathbf{v}_s \cdot \nabla_x f_s + \frac{q_s}{m_s} (\mathbf{E} + \mathbf{v}_s \times \mathbf{B}) \cdot \nabla_{\mathbf{v}_s} f_s = 0, \quad (13)$$

$$\lambda^2 \partial_t^2 \mathbf{E} + \bar{\rho} \mathbf{E} + \lambda^2 c^2 \nabla \times \nabla \times \mathbf{E} = \nabla \cdot \bar{\mathbf{P}} - \bar{\mathbf{J}} \times \mathbf{B}, \quad (14)$$

$$\partial_t \mathbf{B} + \nabla \times \mathbf{E} = 0. \quad (15)$$

The reformulated VM system, consisting of Eqs. (13), (14), and (15), is equivalent to the original VM system represented by Eqs. (5), (6), and (7) [3]. Importantly, the reformulated VM system retains the ability to provide solutions even in the quasi-neutral limit $\lambda \rightarrow 0$. In this limit, Eq. (14) simplifies to the following form,

$$\bar{\rho} \mathbf{E} + \nabla \times \nabla \times \mathbf{E} = \nabla \cdot \bar{\mathbf{P}} - \bar{\mathbf{J}} \times \mathbf{B}, \quad (16)$$

where the electric field \mathbf{E} can be directly obtained. Combined Eq. (16) with the generalized Ohm's law Eq. (11) and Faraday's law (15), it can be observed that $\mathbf{J} = \nabla \times \mathbf{B}$, implying that the plasma is in a quasi-neutral state.

Obviously, the reformulated VM system (13), (14) and (15) provides a more straightforward way for the investigation of the quasi-neutral limit. Consequently, in the remaining part of this paper, we will develop the kinetic scheme based on the reformulated VM system (13), (14), and (15) rather than the VM system (5), (6), and (7). For the traditional explicit Eulerian scheme, the numerical time step is determined by $\Delta t = \min(\Delta t_c, \Delta t_\lambda)$, where Δt_c represents the restriction imposed by the CFL condition, and Δt_λ represents the restriction imposed by the plasma period w_p^{-1} (equivalent to the normalized Debye length λ). Additionally, Δt_c is further limited by the transport velocity \mathbf{v}_s and electromagnetic force $\frac{q_s}{m_s} (\mathbf{E} + \mathbf{v}_s \times \mathbf{B})$ in the Vlasov equation, as well as by the speed of light c in the Maxwell equation. These constraints in Δt_c can be overcome by employing the semi-Lagrangian method and an implicit field solver, as demonstrated in our previous study [16].

In the following section, we aim to develop an asymptotic-preserving conservative semi-Lagrangian scheme for the reformulated VM system (13), (14) and (15), which enables simultaneous and seamless simulation of the electromagnetic plasma in both non-neutral regimes ($\lambda \sim O(1)$) and quasi-neutral regimes ($\lambda \rightarrow 0$), while avoiding limitations on the numerical time step induced by the CFL condition and the plasma period λ .

3. Numerical methods

In this section, we will present the asymptotic-preserving conservative semi-Lagrangian scheme, named CSL-RME, which is based on the CSL and RME. The CSL-RME is designed for solving the reformulated VM system (13), (14), and (15). The proposed method involves several key steps, including the update rule for the reformulated VM system, the CSL scheme for Vlasov equation, and the electromagnetic field evaluation.

3.1. Update rule

In order to solve the multi-dimensional reformulated VM system, we firstly split Vlasov Eq. (13) as follows,

$$\partial_t f_s + \mathbf{v}_s \cdot \nabla_x f_s = 0, \quad (17)$$

$$\partial_t f_s + \frac{q_s}{m_s} (\mathbf{E} + \mathbf{v}_s \times \mathbf{B}) \cdot \nabla_{\mathbf{v}_s} f_s = 0. \quad (18)$$

Moreover, to achieve second-order accuracy in time, Eq. (13) can be discretized using the Strang splitting method. This involves solving Eq. (17) for a half time step, followed by solving Eq. (18) for a full time step, and finally solving Eq. (17) for a second half time step. Specifically, the numerical update from $f_s^k(\mathbf{x}, \mathbf{v})$ (the solution at $t^k = k\Delta t$) to $f_s^{k+1}(\mathbf{x}, \mathbf{v})$ can be expressed as follows,

$$f_s^*(\mathbf{x}, \mathbf{v}) = f_s^k(\mathbf{x} - \theta \Delta t \mathbf{v}, \mathbf{v}), \quad (19)$$

$$f_s^{**}(\mathbf{x}, \mathbf{v}) = f_s^* \left(\mathbf{x}, \mathbf{v} - \frac{q_s}{m_s} (\mathbf{E}^{k+\theta} + \mathbf{v} \times \mathbf{B}^{k+\theta}) \Delta t \right), \quad (20)$$

$$f_s^{k+1}(\mathbf{x}, \mathbf{v}) = f_s^{**}(\mathbf{x} - (1 - \theta) \Delta t \mathbf{v}, \mathbf{v}), \quad (21)$$

which maintain second-order temporal accuracy when $\theta = 1/2$. Eqs. (19) and (21) describe plasma transport in physics space and can be exactly solved using Lie splitting operators in each dimension, while Eq. (20) does not possess the same property due to the non-commutativity of the splitting operators in velocity space, resulting from the presence of the magnetic field. If second-order temporal accuracy for the entire system is desired, the Strang splitting method can be employed once again for Eq. (20). Alternatively, other methods can be used [33,53,54]. Then the multi-dimensional Vlasov Eq. (13) is reduced to a succession of one-dimensional problems. This choice not only provides more alternative methods to solve Vlasov Eq. (13), but also makes the multi-dimensional simulation to be more practical.

Besides, electric field Eq. (14) is discretized as follows,

$$\frac{\lambda^2}{\theta^2 \Delta t^2} \left(\mathbf{E}_j^{k+\theta} - 2\mathbf{E}_j^k + \mathbf{E}_j^{k-\theta} \right) + \bar{\rho}_j^k \mathbf{E}_j^{k+\theta} + \lambda^2 c^2 \nabla \times \nabla \times \mathbf{E}_j^{k+\theta} = \nabla \cdot \bar{\mathbf{P}}_j^k - \bar{\mathbf{J}}_j^{k+\theta} \times \mathbf{B}_j^k, \quad (22)$$

where second-order temporal derivative of the electric field is discretized using a central differencing scheme, and the implicit electric field $\mathbf{E}^{k+\theta}$ and current density $\bar{\mathbf{J}}^{k+\theta}$ with $\theta \geq 1/2$ are used to eliminate the strict numerical stability constraints related to the fastest electron response time, i.e., the electron plasma period λ .

Once $\mathbf{E}^{k+\theta}$ is known, the magnetic field can be obtained using Faraday's equation (15) as follows:

$$\mathbf{B}^{k+1} = \mathbf{B}^k - \Delta t \nabla \times \mathbf{E}^{k+\theta}. \quad (23)$$

Now, the key is to determine the time evolution of the velocity distribution function $f_s^{k+1}(\mathbf{x}, \mathbf{v})$, as well as the electromagnetic fields $\mathbf{E}^{k+\theta}$ and $\mathbf{B}^{k+\theta}$.

3.2. Conservative semi-Lagrangian scheme

In this section, we present the method to solve the kinetic transport equations (19), (20), and (21) by expressing them in the following unified form:

$$\partial_t f_s + \partial_x (a f_s) = 0. \quad (24)$$

In the Eqs. (19) and (21), a represents the discrete velocity \mathbf{v} , while in Eq. (20), it represents the electromagnetic force $\frac{q_s}{m_s} (\mathbf{E} + \mathbf{v} \times \mathbf{B})$. The linear hyperbolic Eq. (24) enables the implementation of a conservative scheme based on the characteristics lines. To solve Eq. (24), we employ the CSL scheme [16,24], a positive flux-conservative (PFC) approach that conserves mass while accurately tracking particle trajectories over time. For completeness, we summarize the key aspects of the CSL scheme below:

First, we introduce a set of mesh points $\{x_{j+1/2}\}_{I_j}$ that span the computational domain $[x_{\min}, x_{\max}]$. Each mesh point is associated with a uniform numerical cell $I_j = [x_{j-1/2}, x_{j+1/2}]$ centered at $x_j = (x_{j-1/2} + x_{j+1/2})/2$, with a cell size of $\Delta x_j = x_{j+1/2} - x_{j-1/2}$. We use $f_j^k = \frac{1}{\Delta x} \int_{x_{j-1/2}}^{x_{j+1/2}} f(x, t^k) dx$ to represent the cell average of the solution within the cell I_j . By tracing the characteristic lines backwards, starting from the cell $[x_{j-1/2}, x_{j+1/2}]$, we can determine the upstream cell as $[x_{j-1/2} - a\Delta t, x_{j+1/2} - a\Delta t]$, denoted as $[x_{j-1/2}^*, x_{j+1/2}^*]$. Utilizing the conservation property of Eq. (24), we obtain the following relationship,

$$\int_{x_{j-1/2}}^{x_{j+1/2}} f(x, t^{k+1}) dx = \int_{x_{j-1/2}^*}^{x_{j+1/2}^*} f(x, t^k) dx,$$

which can be rewritten in the following flux form,

$$f_j^{k+1} = f_j^k + F_{j-1/2} - F_{j+1/2}, \quad (25)$$

where $F_{j-1/2} = \frac{1}{\Delta x} \int_{x_{j-1/2} - a\Delta t}^{x_{j-1/2}} f^k dx$ and $F_{j+1/2} = \frac{1}{\Delta x} \int_{x_{j+1/2} - a\Delta t}^{x_{j+1/2}} f^k dx$.

Then we present the flux $F_{j+1/2}$ in the third order scheme in the case of $\varphi < 1$ and $a > 0$ [24],

$$F_{j+1/2} = \left(f_j^k + \frac{1}{6} (2 - |\varphi|)(1 - |\varphi|) (f_{j+1}^k - f_j^k) + \frac{1}{6} (1 - |\varphi|)(1 + |\varphi|) (f_j^k - f_{j-1}^k) \right) \varphi, \quad (26)$$

where $\varphi = a\Delta t/\Delta x$ is related to CFL condition. Note that when $a \leq 0$, the procedure described above exhibits mirror symmetry with respect to x_j . Additionally, for $\varphi \geq 1$, the case can be handled by performing whole grids shift, followed by considering the cases where $\varphi < 1$.

To preserve the positivity of the distribution function and maintain the high-order accuracy, we adopt a general high-order parametrized positivity-preserving (PP) limiter in [18]. The key ingredient is to modify the high order numerical flux towards the first order monotone flux as follows,

$$\hat{F}_{j+1/2} = \varepsilon_{j+1/2} (F_{j+1/2} - f_{j+1/2}) + f_{j+1/2}, \quad (27)$$

where $f_{j+1/2} = \varphi f_j^k$ is the first order flux, and $\varepsilon_{j+1/2} \in [0, 1]$ is the positivity-preserving limiter to ensure the positivity of the function f_j^{k+1} in Eq. (25). Further details on deriving $\varepsilon_{j+1/2}$ can be found in [16,18].

Finally, we replace the flux $F_{j\pm 1/2}$ in Eq. (25) with the modified flux $\hat{F}_{j\pm 1/2}$ in Eq. (27). As a result, the distribution function f_j^{k+1} is updated by

$$f_j^{k+1} = f_j^k + \hat{F}_{j-1/2} - \hat{F}_{j+1/2}, \quad (28)$$

By incorporating the third-order PFC scheme [24] and the general high-order PP limiter [18] into the current CSL scheme, we achieve exact preservation of mass and positivity of the distribution function with third-order spatial accuracy [16]. Additionally, the current CSL scheme eliminates the CFL restriction, allowing for larger time steps while maintaining accuracy.

3.3. Electromagnetic field evaluation

In this section, we discretize Eq. (22) to evaluate the electric field $E_j^{k+\theta}$ within the physics cell j . It is evident that Eq. (22) represents a second-order partial differential equation in time. To eliminate the presence of the electric field $E_j^{k-\theta}$ in Eq. (22), we take into account the Ampère's law, which can be expressed as follows,

$$\lambda^2 c^2 \nabla \times \mathbf{B}_j^k - \mathbf{J}_j^k = \frac{\lambda^2}{\theta \Delta t} (\mathbf{E}_j^k - \mathbf{E}_j^{k-\theta}). \quad (29)$$

By substituting Eq. (29) into Eq. (22), we can obtain

$$\frac{\lambda^2}{\Delta t^2} \mathbf{E}_j^{k+\theta} + \lambda^2 c^2 \theta^2 \nabla \times \nabla \times \mathbf{E}_j^{k+\theta} = \frac{\lambda^2}{\Delta t^2} \mathbf{E}_j^k + \frac{\lambda^2 c^2 \theta}{\Delta t} \nabla \times \mathbf{B}_j^k - \frac{\theta}{\Delta t} \mathbf{J}_j^{k+\theta}, \quad (30)$$

where $\mathbf{J}_j^{k+\theta}$ represents the total current density at time $t^{k+\theta}$, and it is defined as,

$$\mathbf{J}_j^{k+\theta} = \mathbf{J}_j^k + \theta \Delta t (\bar{\rho}_j^k \mathbf{E}_j^{k+\theta} + \bar{\mathbf{J}}_j^{k+\theta} \times \mathbf{B}_j^k - \nabla \cdot \bar{\mathbf{P}}_j^k). \quad (31)$$

Similar to Eq. (31), the current density $\mathbf{J}_{s,j}^{k+\theta}$ for each species s at $t^{k+\theta}$ can be expressed as,

$$\mathbf{J}_{s,j}^{k+\theta} = \mathbf{J}_{s,j}^{k*} + \frac{q_s \theta \Delta t}{m_s} (\rho_{s,j}^k \mathbf{E}_j^{k+\theta} + \mathbf{J}_{s,j}^{k+\theta} \times \mathbf{B}_j^k), \quad (32)$$

where

$$\mathbf{J}_{s,j}^{k*} = \mathbf{J}_{s,j}^k - \theta \Delta t \nabla \cdot \mathbf{P}_{s,j}^k. \quad (33)$$

In practical computations, when considering the transport Eq. (19) in physics space, we can further rewrite Eq. (33) as $\mathbf{J}_{s,j}^{k*} = \int_{\Omega_v} \mathbf{v}_s \cdot f_{s,j}^* d\mathbf{v}$. This formulation avoids the computation of the pressure tensor $\mathbf{P}_{s,j}^k$ [16]. Note that $\mathbf{J}_{s,j}^k$ represents the current density at the beginning of plasma transport in physics space in Eq. (19), while $\mathbf{J}_{s,j}^{k*}$ represents it at the end of this transport process.

By explicitly expressing the current density $\mathbf{J}_{s,j}^{k+\theta}$ for each species s in Eq. (32), we can represent the total current density $\mathbf{J}_j^{k+\theta}$ in Eq. (31) as follows,

$$\mathbf{J}_j^{k+\theta} = \hat{\mathbf{J}}_j^{k+\theta} + \theta \Delta t \boldsymbol{\mu}_j^k \cdot \mathbf{E}_j^{k+\theta}, \quad (34)$$

where

$$\hat{\mathbf{J}}_j^{k+\theta} = \sum_s \boldsymbol{\alpha}_{s,j}^k \cdot \mathbf{J}_{s,j}^{k*}, \quad (35)$$

$$\boldsymbol{\mu}_j^k = \sum_s \frac{q_s \rho_{s,j}^k}{m_s} \boldsymbol{\alpha}_{s,j}^k. \quad (36)$$

Here, the effective dielectric tensor $\boldsymbol{\mu}_j^k$ accounts for the feedback of the electric field on the plasma current and density [2]. On the other hand, the transformation tensor operator $\boldsymbol{\alpha}_{s,j}^k$ represents a rotation of the current density and is defined as follows,

$$\alpha_{s,j}^k = \frac{1}{1 + (\varepsilon_s \mathbf{B}_j^k)^2} (\mathbf{I} - \varepsilon_s \mathbf{I} \times \mathbf{B}_j^k + \varepsilon_s^2 \mathbf{B}_j^k \mathbf{B}_j^k), \quad (37)$$

where \mathbf{I} is the identity matrix and $\varepsilon_s = q_s \theta \Delta t / m_s$. Unlike the method in Degond et al. [3], where Eq. (32) explicitly uses $\mathbf{J}_{s,j}^k \times \mathbf{B}_j^k$ on the right-hand side, we adopt a semi-implicit approach by employing $\mathbf{J}_{s,j}^{k+\theta} \times \mathbf{B}_j^k$, which introduces the rotation matrix $\alpha_{s,j}^k$ (37). Although this makes the current method slightly more complex, it enhances stability in the presence of strong magnetic fields, as demonstrated by the iPic3D method [2].

Note that Eq. (34) represents the source term of the Maxwell equation, which couples particle motion and electromagnetic field evolution. This formulation allows the current field solver to consider both the stability of the implicit method (where the numerical time step is not limited by λ) and the efficiency of the explicit method (where there is no need to iteratively solve nonlinear equations). In Eq. (34), $\hat{\mathbf{J}}_j^{k+\theta}$ represents the transformed current flux under the constraint of the magnetic field.

Substituting Eq. (34) into Eq. (30), we obtain the expression for $\mathbf{E}_j^{k+\theta}$ as follows,

$$\frac{\lambda^2}{\Delta t^2} \mathbf{E}_j^{k+\theta} + \theta^2 \boldsymbol{\mu}^k \cdot \mathbf{E}_j^{k+\theta} + \lambda^2 c^2 \theta^2 \nabla \times \nabla \times \mathbf{E}_j^{k+\theta} = \frac{\lambda^2}{\Delta t^2} \mathbf{E}_j^k + \frac{\lambda^2 c^2 \theta}{\Delta t} \nabla \times \mathbf{B}_j^k - \frac{\theta}{\Delta t} \hat{\mathbf{J}}_j^{k+\theta}. \quad (38)$$

The expression $\theta^2 \boldsymbol{\mu}^k \cdot \mathbf{E}_j^{k+\theta}$ in Eq. (38), resulting from the final term in Eq. (34), represents a combination of scaling and rotational transformations on the future value of the electric field. When fast plasma oscillation periods cannot be resolved due to a large time step (i.e., $\lambda < \Delta t$), this term becomes dominant and effectively suppresses the rapid growth of the electric field.

Once $\mathbf{E}_j^{k+\theta}$ is provided, the magnetic field \mathbf{B}_j^{k+1} can be determined by using Eq. (23). Subsequently, we obtain the magnetic field $\mathbf{B}_j^{k+\theta}$,

$$\mathbf{B}_j^{k+\theta} = \theta \mathbf{B}_j^{k+1} + (1 - \theta) \mathbf{B}_j^k, \quad (39)$$

and the electric field \mathbf{E}_j^{k+1} ,

$$\mathbf{E}_j^{k+1} = (\mathbf{E}_j^{k+\theta} - \mathbf{E}_j^k) / \theta + \mathbf{E}_j^k, \quad (40)$$

After solving the field equation, in order to avoid the generation of non-physics charge separation in the electric field \mathbf{E}_j^{k+1} , a correction of electric field, namely Boris correction [3,51], is employed to enforce the Gauss's Law [2,3],

$$\tilde{\mathbf{E}}_j^{k+1} = \mathbf{E}_j^{k+1} - \nabla \phi_j^{k+1}, \quad (41)$$

where $\tilde{\mathbf{E}}_j^{k+1}$ is the corrected electric field, and ϕ_j^{k+1} denotes the electric potential to be determined. Additionally, Gauss's law is considered and given by,

$$\lambda^2 \nabla \cdot \tilde{\mathbf{E}}_j^{k+1} = \tilde{\rho}_j^{k+1}, \quad (42)$$

where $\tilde{\rho}_j^{k+1} = \rho_j^k + \Delta t \nabla \cdot \tilde{\mathbf{J}}_j^{k+1}$ is obtained from the continuity equation. Similar to Eq. (34), we can determine that $\tilde{\mathbf{J}}_j^{k+1} = \hat{\mathbf{J}}_j^{k+1} + \Delta t \boldsymbol{\mu}_j^k \cdot \tilde{\mathbf{E}}_j^{k+1}$. Therefore, by combining Eqs. (41) and (42), we can derive the electric potential ϕ_j^{k+1} as follows,

$$-\nabla \cdot \left[\left(\frac{\lambda^2}{\Delta t^2} \mathbf{I} + \boldsymbol{\mu}_j^k \right) \cdot \nabla \phi_j^{k+1} \right] = \frac{\rho_j^k}{\Delta t^2} - \nabla \cdot \left[\left(\frac{\lambda^2}{\Delta t^2} \mathbf{I} + \boldsymbol{\mu}_j^k \right) \cdot \mathbf{E}_j^{k+1} \right] - \frac{1}{\Delta t} \nabla \cdot \hat{\mathbf{J}}_j^{k+1}. \quad (43)$$

Additionally, taking Ampère's law into consideration, we have,

$$\lambda^2 (\mathbf{E}_j^{k+1} - \mathbf{E}_j^k - \Delta t c^2 \nabla \times \mathbf{B}_j^{k+1}) = -\Delta t \mathbf{J}_j^{k+1}. \quad (44)$$

By combining Eq. (34) and taking the divergence of both sides of Eq. (44), while considering the condition $\nabla \cdot (\nabla \times \mathbf{B}) = 0$, Eq. (43) can be simplified as follows,

$$-\nabla \cdot \left[\left(\lambda^2 \mathbf{I} + \Delta t^2 \boldsymbol{\mu}_j^k \right) \cdot \nabla \phi_j^{k+1} \right] = \rho_j^k - \lambda^2 \nabla \cdot \mathbf{E}_j^k. \quad (45)$$

The right-hand side of Eq. (45) represents the difference between the charge density ρ_j^k and the electric field \mathbf{E}_j^k obtained from the field solver, which is used to assess the inconsistency of Gauss's law. The primary objective of Eq. (45) is to gradually eliminate this inconsistency and suppress non-physics charge separation as the evolution progresses [2,3]. In practical computations, when considering Gauss's law correction, Eq. (45) is utilized to determine the corrected potential ϕ_j^{k+1} , and Eq. (41) is used to obtain the corrected electric field $\tilde{\mathbf{E}}_j^{k+1}$. Finally, the electric field is updated by assigning $\mathbf{E}_j^{k+1} = \tilde{\mathbf{E}}_j^{k+1}$.

By employing Eq. (38), the electric field $\mathbf{E}_j^{k+\theta}$ is solved to ensure that the numerical time step in the current CSL-RME is not limited by normalized Debye length λ . Furthermore, Eq. (45) is used to correct the electric field \mathbf{E}_j^{k+1} in order to satisfy Gauss's law, providing a more reasonable solution.

3.4. Algorithm

To provide a clearer understanding of the proposed CSL-RME, we present its evolution procedure. The method evolves from the initial distribution function f_s^k and electromagnetic field E^k and B^k , progressing from time t^k to t^{k+1} through the following steps:

- (1) Calculate function f_s^* from f_s^k by solving Eq. (19) with Lie Splitting in physics space for $\Delta t/2$.
 - (a) Compute the flux according to Eq. (26) in each physics direction;
 - (b) Correct the flux with parametrized PP limiter by Eq. (27) in each physics direction;
 - (c) Obtain function f_s^* Eq. (28) in each physics direction.
- (2) Update the electromagnetic field with a time step Δt .
 - (a) Obtain the current density $\hat{J}_j^{k+\theta}$ and the dielectric tensor μ_j^k using Eqs. (35) and (36), respectively.
 - (b) Solve Eq. (38) to obtain the electric field $E_j^{k+\theta}$, and update the electric field E_j^{k+1} with Eq. (40);
 - (c) Update the magnetic field B_j^{k+1} using Eq. (23), and calculate $B_j^{k+\theta}$ using Eq. (39);
 - (d) If Gauss's law is enforced, the electric field \tilde{E}_j^{k+1} is corrected using Eq. (41), and update the electric field $E_j^{k+1} = \tilde{E}_j^{k+1}$, where the corrected electric potential ϕ_j^{k+1} is obtained from Eq. (45).
- (3) Update f_s^{**} by solving Eq. (20) with Strang Splitting in velocity space for Δt .
- (4) Update f_s^{k+1} by solving Eq. (21) with Lie Splitting in physics space for $\Delta t/2$.

It is worth noting that the process of steps (3) and (4) in each dimension is similar to that of step (1), and they are omitted here for the sake of presentation simplicity. If Gauss's law is not enforced, step (2)(d) can be skipped. We employ the finite element method [55] along with the GMRES solver to solve the linear system described in Eq. (38). Specifically, a third-order spatial accuracy finite element field solver is employed in this paper, and the computational procedure, along with the treatment of boundary conditions, is detailed in [16]. Although any value $\theta \geq 1/2$ can be chosen, unless otherwise specified, the parameter θ will be set to $1/2$ in current paper.

4. Analysis of CSL-RME

In this section, we will discuss three important aspects on the proposed CSL-RME: asymptotic-preserving (AP) property in the quasi-neutral limit, the behavior in the electrostatic regime, and the comparison with other kinetic methods in plasma simulations.

4.1. AP property in the quasi-neutral limit

First, we demonstrate that the proposed CSL-RME preserves the AP property in the quasi-neutral limit as $\lambda \rightarrow 0$. As stated in Ref. [3,40], a kinetic scheme is considered AP if it satisfies (a) it is consistent with S_ϵ when the numerical parameters (such as Δx and Δt) resolve the scales associated with ϵ ; (b) it is consistent with S_0 when $\epsilon \rightarrow 0$, and the choice of Δx and Δt is not restricted by ϵ . In this paper, S_ϵ is the reformulated VM system (13), (14) and (15), while S_0 is the system dependent on λ . It is not difficult to verify that the proposed CSL-RME satisfies condition (a), since it was derived from the reformulated VM system. The main task is to verify whether the scheme satisfies condition (b) or not.

If the initial conditions satisfy quasi-neutrality, i.e., $\rho^0 = 0$ and $\mathbf{J}^0 = \nabla \times \mathbf{B}^0$, in the quasi-neutral limit $\lambda \rightarrow 0$, the evolution equation for the electric field Eq. (38) can be expressed as

$$\theta \Delta t \mu_j^k \cdot E_j^{k+\theta} + \theta \Delta t \nabla \times \nabla \times E_j^{k+\theta} = \nabla \times B_j^k - \hat{J}_j^{k+\theta}, \quad (46)$$

Taking into consideration Eq. (31) and Eq. (34), along with the relationship $\mathbf{J}_j^k = \nabla \times \mathbf{B}_j^k$, the expression for the electric field in Eq. (46) can be further simplified as follows:

$$\bar{\rho}_j^k E_j^{k+\theta} + \nabla \times \nabla \times E_j^{k+\theta} = \nabla \cdot \bar{P}_j^k - \bar{J}_j^{k+\theta} \times B_j^k, \quad (47)$$

which represents the consistent discretization format of the quasi-neutral limit Eq. (16). Encouragingly, Eq. (38) couples particle motion and electromagnetic field evolution in a semi-implicit way, the numerical time step of the current CSL-RME is not limited by λ .

The above analysis demonstrates that in the quasi-neutral limit as $\lambda \rightarrow 0$, the proposed CSL-RME can automatically degenerate to a discretization format consistent with the quasi-neutral system. Moreover, the numerical parameters Δx and Δt are not limited by λ . This means that CSL-RME satisfies condition (b). Therefore, the proposed CSL-RME preserves the AP properties in the quasi-neutral limit, which will be verified in numerical experiments in Section 5.3.

4.2. The behavior in the electrostatic regime

Second, we will discuss the behavior of CSL-RME in the electrostatic regime, characterized by a vanishing magnetic field. In the reformulated VM system (13), (14), and (15), this corresponds to $c^{-1} \rightarrow 0$. In the electrostatic regime, the magnetic field vanishes,

resulting in $\nabla \times \mathbf{B} = 0$ and $\nabla \cdot \mathbf{B} = 0$. Additionally, if there is no magnetic field source at the boundary, we have $\partial_t \mathbf{B} = 0$. Consequently, the Faraday's law Eq. (15) simplifies to $\nabla \times \mathbf{E} = 0$. Thus, electric field Eq. (38) reduces to,

$$\frac{\lambda^2}{\Delta t^2} \mathbf{E}_j^{k+\theta} + \theta^2 \boldsymbol{\mu}^k \cdot \mathbf{E}_j^{k+\theta} = \frac{\lambda^2}{\Delta t^2} \mathbf{E}_j^k - \frac{\theta}{\Delta t} \hat{\mathbf{J}}_j^{k+\theta}. \quad (48)$$

For convenience, we consider $\theta = 1$. It should be noted that Eq. (48) just satisfies Ampère's law. To accurately recover the electrostatic regime, we need to consider Gauss's correction. By combining Eq. (48) with the Gauss-corrected electric potential (45), we obtain,

$$\nabla \cdot \left[\left(\lambda^2 \mathbf{I} + \Delta t^2 \boldsymbol{\mu}_j^k \right) \cdot \nabla \tilde{\phi}_j^{k+1} \right] = \rho_j^k - \Delta t \nabla \cdot \hat{\mathbf{J}}_j^{k+1} \quad (49)$$

where $\nabla \tilde{\phi} = \nabla \phi - \mathbf{E}$. When the magnetic field is zero, the rotation matrix $\alpha_{s,j}^k = \mathbf{I}$ in Eqs. (35) and (36). Therefore, Eq. (49) represents the consistent discretization format of the reformulated Poisson equation in [27].

This analysis indicates that in the absence of a magnetic field, the current CSL-RME, with the Gauss's correction Eq. (45), can automatically revert to a discretization format consistent with the electrostatic system. This will be verified in numerical experiments in Section 5.1.

4.3. Comparison with other kinetic methods

Finally, we discuss some differences between the current CSL-RME and other kinetic methods, especially the implicit methods, in plasma simulations. Implicit methods have been widely used in the Particle-in-Cell (PIC) method but have received less attention in the grid-based method. Here, we focus on comparing the CSL-RME with the AP-PIC method. It's worth noting that the differences between the AP-PIC method and other implicit PIC methods, such as the full implicit method [56,57], implicit moment method [2,6], and direct implicit method [58,59], have been systematically addressed in Ref [3].

On the one hand, CSL-RME and AP-PIC share some similarities. Similar to the implicit moment method [2,6], both the CSL-RME and AP-PIC employ macroscopic moment equations of the Vlasov equation to predict the sources of the field equations, providing a direct and explicit closure of Maxwell's equations. This approach significantly reduces the computational cost compared to fully implicit methods that require nonlinear iterations, while still maintaining favorable stability properties. However, there are differences in their objectives. While the implicit moment method aims to relax stability conditions, the CSL-RME and AP-PIC strive to be consistent with a well-defined quasi-neutral model and preserve the AP property. The elimination of stability conditions related to the plasma period is a consequence of scaling assumptions made in Section 2.2 to define the quasi-neutral limit, along with the implicit treatment of the electric field and current density in the reformulated VM system.

On the other hand, although CSL-RME and AP-PIC seek the same ends, they differ fundamentally in their approach. CSL-RME is a grid-based kinetic method, while AP-PIC is a particle-based method. As studied in Ref [8], the grid-based method is advantageous in terms of being free from numerical noise, which is particularly beneficial for exploring micro-scale physics and unsteady plasma dynamics, such as plasma waves and plasma turbulence. Additionally, in AP-PIC, only the electric field is implicit in the moment equation, specifically the general Ohm's law. In contrast, both the current density in the Hall term $\hat{\mathbf{J}}_j^{k+\theta} \times \mathbf{B}_j^k$ and the electric field are implicit in CSL-RME. This leads to the formation of the effective dielectric tensor $\boldsymbol{\mu}_j^k$ in Eq. (36), which accounts for the feedback of the electromagnetic field on the plasma current and density [2].

5. Numerical experiments

In this section, we conduct four numerical experiments to validate the proposed CSL-RME, including linear Landau damping (1d2v), Weibel instability (1d2v), plasma opening switch (1d2v), and magnetic reconnection (2d3v). In the first two numerical experiments, only electrons dynamics (assume ions form a uniform static background) are considered, while both electrons and ions dynamics are considered in the last two experiments. For the purpose of comparison, we also present a discretization of the Maxwell equations employed in the traditional explicit kinetic method [16],

$$\frac{\lambda^2}{\Delta t^2} \mathbf{E}_j^{k+\theta} + \lambda^2 c^2 \theta^2 \nabla \times \nabla \times \mathbf{E}_j^{k+\theta} = \frac{\lambda^2}{\Delta t^2} \mathbf{E}_j^k + \frac{\lambda^2 c^2 \theta}{\Delta t} \nabla \times \mathbf{B}_j^k - \frac{\theta}{\Delta t} \mathbf{J}_j^{k+\theta,*}, \quad (50)$$

where $\mathbf{J}_j^{k+\theta,*} = \mathbf{J}_j^{k*} + \theta \Delta t \left(\hat{\rho}_j^k + \hat{\mathbf{J}}_j^k \times \mathbf{B}_j^k \right)$. For convenience, in the following we will use the term 'CSL-RME' to refer to the scheme used for the reformulated VM system, consisting of Eqs. (13), (14), and (15). On the other hand, we will use 'CSL-ME' to denote the scheme used for the original VM system, which includes Eqs. (5), (6), and (7). Note that the CSL-ME follows a similar evolution procedure to CSL-RME, as described in Section 4.3, except that the electric field is obtained using Eq. (50) instead of Eq. (38).

Furthermore, we mention that the time step Δt in CSL-ME should be chosen to resolve the plasma period ω_p^{-1} , which is equivalent to the value of the normalized Debye length λ . It is worth noting that in this paper, the proposed kinetic method specifically refers to CSL-RME, while CSL-ME is used for comparison purposes. For the sake of clarity, we specify the specific version of the original VM system (5), (6), and (7) used for each problem. The conversion from Eq. (6) to Eq. (50) or Eq. (38) is straightforward, and we omit the details here. Unless explicitly mentioned, all simulations assume periodic boundary conditions for the velocity distribution functions in velocity space, and the parameter θ is set to 1/2.

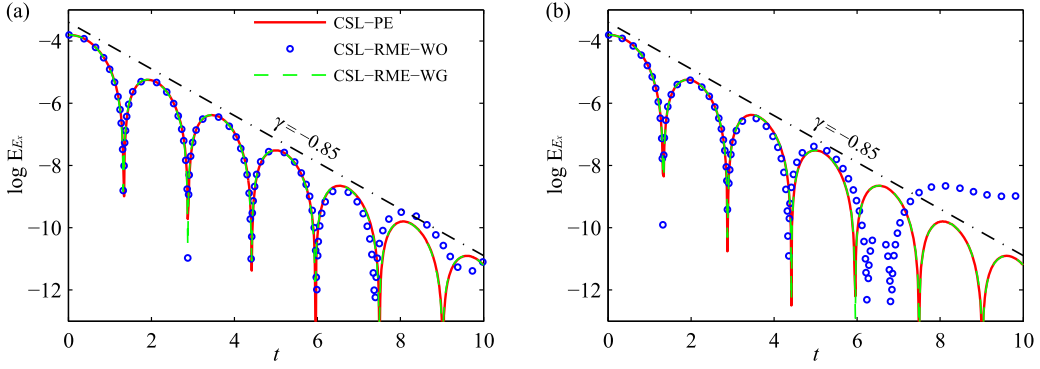


Fig. 1. Linear damping: $C = 1$. Time evolution of electric field energy E_{E_x} for Landau damping with $\theta = 1/2$ (a) and $\theta = 1$ (b).

Table 1
The L^2 error and convergence order in space for Landau damping with $\Delta t = 0.5(\Delta x/v_{x_m})^{3/2}$.

V	$N = 8^3$		$N = 16^3$		$N = 32^3$		$N = 64^3$	
	L^2 error	Order						
f	1.07×10^{-2}	—	1.35×10^{-3}	2.98	1.58×10^{-4}	3.09	1.89×10^{-5}	3.06
E_x	1.06×10^{-2}	—	1.29×10^{-3}	3.03	1.52×10^{-4}	3.08	1.68×10^{-5}	3.17

5.1. Landau damping

In this subsection, the classical linear Landau damping is utilized to validate the CSL-RME scheme with two main purposes. Firstly, we investigate whether the solution of CSL-RME in the electrostatic regime is consistent with that of the electrostatic model. Secondly, we examine the accuracy of CSL-RME.

Considering the problem with 1-D physics space and 2-D velocity space (1d2v), where the electric field components are denoted as E_x and E_y , and the magnetic field component is denoted as B_z , the VM system can be simplified as follows,

$$\begin{aligned} \partial_t f_s + v_x \partial_x f_s + \frac{q_s}{m_s} (E_x + v_y B_z) \partial_{v_x} f_s + \frac{q_s}{m_s} (E_y - v_x B_z) \partial_{v_y} f_s &= 0, \\ \lambda^2 \partial_t E_x &= -J_x, \quad \lambda^2 \partial_t E_y = -\lambda^2 c^2 \partial_x B_z - J_y, \quad \partial_t B_z = -\partial_x E_y. \end{aligned} \tag{51}$$

As in [54], we assume ions are uniformly in the background, and only consider the electrons dynamics, and the initial velocity distribution function of electrons follows,

$$f_e(x, v_x, v_y, 0) = \frac{1}{\pi \beta} \exp \left[- (v_x^2 + v_y^2) / \beta \right] (1 + \alpha_0 \sin(kx)).$$

The initial electric field E_x is solved by the Poisson equation, and the initial electric field E_y and magnetic field B_z are set to zero,

$$\lambda^2 E_x(x, 0) = 1 - n_e, \quad E_y(x, 0) = 0, \quad B_z(x, 0) = 0.$$

In our simulations, we set $\alpha_0 = 0.01$, $k = 1$, $\beta = 2$, $\lambda = 1$, and $c = 1$. The phase space is defined as $[0, L_x] \times [-v_{x_m}, v_{x_m}] \times [-v_{y_m}, v_{y_m}]$, with grids $N = N_x \times N_{v_x} \times N_{v_y}$, where $L_x = 2\pi/k$, $N_x = 64$, $v_{x_m} = v_{y_m} = 6$, and $N_{v_x} = N_{v_y} = 64$. The time stepping size is $\Delta t = C \Delta x / v_{x_m}$, where the CFL number $C = 1$. The boundary conditions of the physics space are periodic.

Fig. 1 presents the time evolution of the electric energy E_{E_x} , where $E_{E_x} = \frac{1}{2} \int |E_x|^2 dx$. In the figure, the black dotted line represents the theoretical decay line with a slope of $\gamma = -0.85$ [52]. CSL-PE denotes the reference solution obtained by solving for E_x using the Poisson equation, while setting E_y and B_z to zero. CSL-RME-WO and CSL-RME-WG are numerical solutions obtained using CSL-RME without and with the Gauss correction given by Eq. (45), respectively. In Fig. 1 (a), for $\theta = 1/2$, it can be observed that after $t > 8$, the electric energy predicted by CSL-RME-WO deviates from the CSL-PE solution. This deviation occurs due to the violation of Gauss's law, leading to non-physics charge separation. When $\theta = 1$ as shown in Fig. 1 (b), the deviation becomes more pronounced. This is because now the numerical time step in the physics space is twice that of $\theta = 1/2$, which worsens the satisfaction of the continuity equation and leads to a poorer approximation of Gauss's law. Encouragingly, CSL-RME-WG with $\theta = 1/2$ or $\theta = 1$ provides results consistent with CSL-PE solutions, thanks to incorporating the electric correction to enforce Gauss's law. The results in Fig. 1 highlight the necessity of the Gauss Law correction in the electrostatic regime. Hence, in the following subsections, unless otherwise specified, CSL-RME refers to CSL-RME-WG with $\theta = 1/2$.

To verify the accuracy and effectiveness of the proposed CSL-RME, we conduct a spatial convergence test. Table 1 presents the L^2 spatial discretization errors and the corresponding convergence orders. To ensure consistency between spatial and temporal accuracy, the time step is set as $\Delta t = 0.5(\Delta x/v_{x_m})^{3/2}$. The L^2 error is calculated by comparing the numerical solutions with the

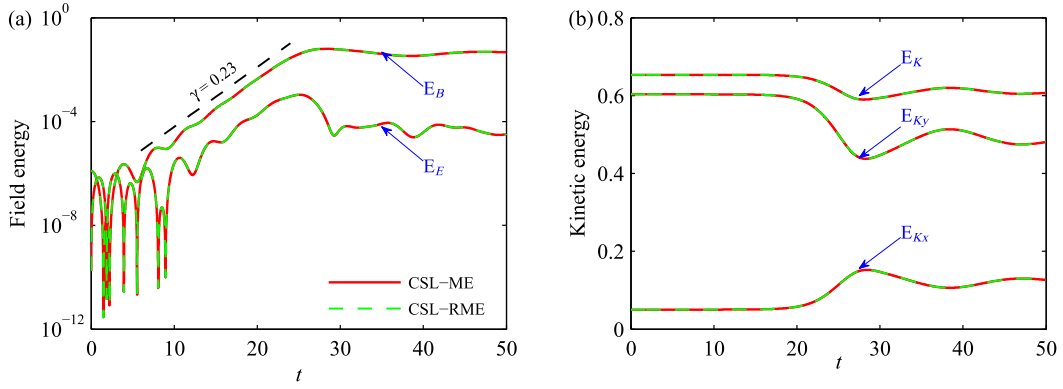


Fig. 2. Weibel instability: $C = 1$. Time evolution of field energy (a) and kinetic energy (b).

reference solutions [16], where the reference solutions are derived using the reversibility of the VM system [60]. Specifically, the simulation starts with initial conditions $f(x, \mathbf{v}, 0)$, $\mathbf{E}(x, 0)$, and $\mathbf{B}(x, 0)$. Running the code, we obtain the numerical solutions $f(x, \mathbf{v}, t)$, $\mathbf{E}(x, t)$, and $\mathbf{B}(x, t)$ at a specific time t . If we choose $f(x, -\mathbf{v}, t)$, $\mathbf{E}(x, t)$, and $-\mathbf{B}(x, t)$ as the initial conditions at time t , the numerical solution at $2t$ should ideally recover $f(x, -\mathbf{v}, 0)$, $\mathbf{E}(x, 0)$, and $-\mathbf{B}(x, 0)$. In this test, we run the simulation up to $t = 10$ and then return to $t = 0$. The results in Table 1 demonstrate the expected third-order accuracy.

The above arguments demonstrate that the proposed CSL-RME, incorporating the Gauss correction, ensures the restoration of physically consistent solutions in the electrostatic regime while mitigating non-physics charge separation. Moreover, CSL-RME achieves third-order accuracy in space, facilitating the prediction of highly accurate solutions.

5.2. Weibel instability

In this section, the proposed method is applied to simulate the Weibel instability for two main purposes. Firstly, we aim to assess the consistency of the results obtained by CSL-RME with those of CSL-ME when the Debye scale λ is well resolved. Secondly, we investigate the performance of the proposed CSL-RME in terms of conservation properties and efficiency.

Here we consider a reduced 1d2v VM system, corresponding to the governing equation given by Eq. (51). We focus on the motion of electrons only, and the initial electron distribution function is [42,61,62],

$$f_e(x, v_x, v_y, 0) = \frac{1}{\pi\beta\sqrt{T_r}} \exp\left[-(v_x^2 + v_y^2/T_r)/\beta\right],$$

and the initial electromagnetic field is,

$$E_x(x, 0) = 0, \quad E_y(x, 0) = 0, \quad B_z(x, 0) = \alpha_0 \sin(kx).$$

In our simulation, we set the perturbation coefficient $\alpha_0 = 10^{-3}$, wave number $k = 1.25$, thermal velocity $\beta = 0.04$, and temperature ratio $T_r = 12$. The normalized Debye length is $\lambda = 1$, and the speed of light is $c = 1$. The phase space is defined as $[0, L_x] \times [-v_{x_m}, v_{x_m}] \times [-v_{y_m}, v_{y_m}]$, where $L_x = 2\pi/k$ represents the length of the physics space, and $v_{x_m} = 1.2$ and $v_{y_m} = 4.14$ define the range of the velocity space. The physics space is discretized with a grid size of N_x , while the velocity space has a grid size of $N_{v_x} \times N_{v_y}$. We apply periodic boundary conditions in the physics space. The time step size is determined as $\Delta t = C\Delta x/v_{y_m}$, and the simulation time is set to 50. Unless otherwise specified, we use $N_x = N_{v_x} = N_{v_y} = 128$ and a CFL number of $C = 1$.

First, we evaluate the accuracy of CSL-RME in comparison to CSL-ME using the default simulation parameters mentioned above, where the normalized Debye length and plasma oscillation period are well resolved ($\Delta x = 0.04\lambda$ and $\Delta t = 0.01\lambda$). In Fig. 2 we plot the time evolution of field energy and kinetic energy. The electric energy E_E is defined as the sum of E_{E_x} and E_{E_y} , where $E_{E_x} = \frac{1}{2} \int |E_x|^2 dx$ and $E_{E_y} = \frac{1}{2} \int |E_y|^2 dx$. The magnetic energy $E_{B_z} = \frac{1}{2} \int |B_z|^2 dx$. The kinetic energy E_K is defined as the sum of E_{K_x} and E_{K_y} , where $E_{K_x} = \frac{1}{2} \int f v_x^2 dx dv_x dv_y$ and $E_{K_y} = \frac{1}{2} \int f v_y^2 dx dv_x dv_y$. Clearly, both the field energy in Fig. 2 (a) and the kinetic energy in Fig. 2 (b) obtained from the proposed CSL-RME agree well with the CSL-ME solutions. The magnetic energy exhibits exponential growth and reaches saturation around $t = 27$. Encouragingly, the growth rate predicted by CSL-RME is $\gamma = 0.23$, which is in good agreement with the theoretical value[61]. In the remaining part of this section, we will focus on presenting the results predicted by CSL-RME, considering their high similarity to the results obtained from CSL-ME.

Then we investigate the performance of proposed CSL-RME in terms of conservation properties, specifically system mass L_1 , moment \mathbf{P} , and total energy E_t , where $L_1 = \int f dx dv_x dv_y$, $\mathbf{P} = \int \mathbf{v} f dx dv_x dv_y + \int \mathbf{E} \times \mathbf{B} dx$, and $E_t = E_K + E_E + E_{B_z}$. To assess the conservation properties, we define the conservation error $|\Delta V| = |V(t) - V(0)|$, where V represents L_1 , P_x , P_y , or E_t . In Fig. 3, we present the time evolution of conservation error for proposed CSL-RME using the fine grids $N = 128^3$, together with the results by using the coarse grids $N = 32^3$. Thanks to the CSL scheme, the system mass L_1 is exactly conserved as expected. Regarding momentum conservation, the proposed CSL-RME demonstrates excellent conservation of P_x , but it does not achieve exact conservation of P_y ,

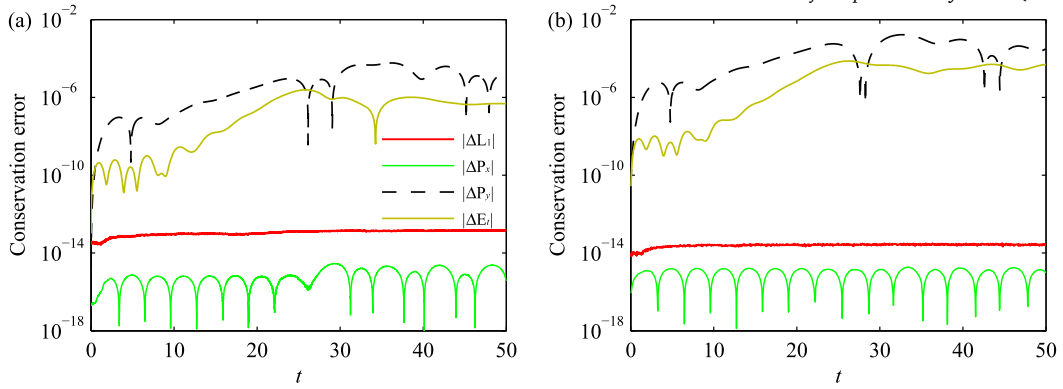


Fig. 3. Weibel instability: $C = 1$. Time evolution of conservation error with fine grids $N_x = 128, N_{v_x} = 128, N_{v_y} = 128$ (a) and coarse grids $N_x = 32, N_{v_x} = 32, N_{v_y} = 32$ (b).

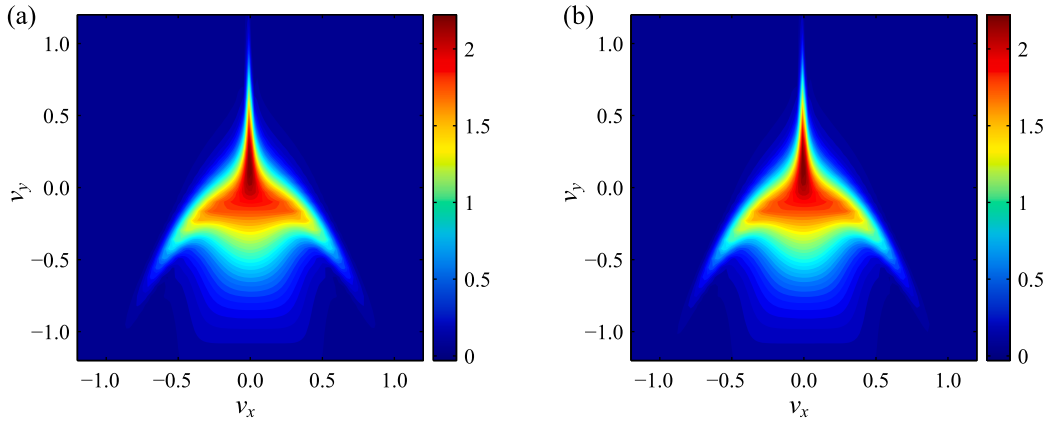


Fig. 4. Weibel instability: $N_x = 128, N_{v_x} = 128, N_{v_y} = 128$. The contour of velocity distribution function at $x = L/2$ and $t = 27$ for $C = 1$ (a) and $C = 10$ (b).

which is consistent with the observations in [16,60,63]. Additionally, it can be observed that the proposed CSL-RME does not achieve exact energy conservation, but the conservation error remains relatively small. Encouragingly, similar conservation errors are also observed in Fig. 3 (b), even when using coarse grids.

In addition to the conservation properties, we are also interested in the efficiency of the CSL-RME, particularly in achieving reasonable physics results with larger time steps. To investigate this, we compare the results obtained with two different CFL numbers, $C = 1$ and $C = 10$, while keeping the grid size constant at $N = 128^3$. Fig. 4 presents the velocity distribution function at $x = L/2$ and $t = 27$ for $C = 1$ and $C = 10$. It is evident from the figure that electrons exhibit a strong anisotropy, leading to different temperatures. This anisotropy plays a crucial role in driving the growth of the magnetic field B_z . Furthermore, it can be observed that the microscopic structure captured by the proposed CSL-RME with $C = 10$ is comparable to the results obtained with $C = 1$, indicating the high accuracy of the proposed method. This suggests that CSL-RME is capable of providing reasonable physics results even with larger time step size, enhancing its computational efficiency.

The above arguments demonstrate that CSL-RME predicts nearly identical results to CSL-ME when the Debye scale is well resolved. Furthermore, the numerical results indicate that the proposed method accurately conserves mass while mimics the moment and energy conservation. Significantly, the proposed CSL-RME exhibits satisfactory performance even when employing larger time step size, which is a highly advantageous feature in the lengthy simulations.

5.3. Plasma opening switch

In this section, we study the dynamics of a practical problem known as the Plasma Opening Switch (POS). The main purpose is to compare the performance of CSL-RME and CSL-ME in different Debye regimes. This comparison aims to illustrate that CSL-RME maintains the AP property in the quasi-neutral limit as λ approaches 0, while CSL-ME does not exhibit such behavior.

POS is a device utilized in pulse power supply systems to deliver a large current in a short timeframe. It consists of a coaxial cylindrical transmission line filled with a high-density plasma. During the switch-on process, charge separation occurs, leading to the formation of a sheath at the plasma boundary. This setup allows for the propagation of electromagnetic waves across the gap, generating extremely high-power pulses. In this section, a simplified 1d2v POS model is employed [3]. The governing equation for this model is represented by Eq. (51), taking into account both electrons and ions dynamics. The physics domain is defined as $[0, L]$,

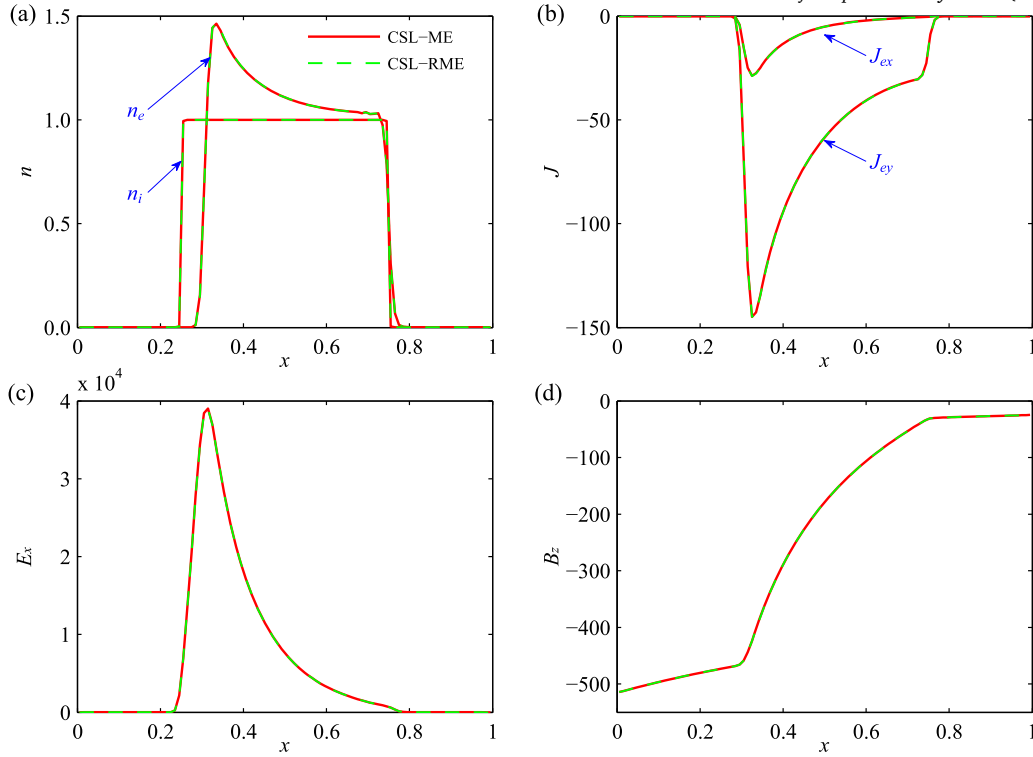


Fig. 5. POS: $\lambda = 1.2 \times 10^{-3}$. The plasma density n (a), current density J (b), electric field E_x (c) and magnetic field B_z (d) against physics space x at $t = 0.02$.

where $L = 0.2$ m. Initially, the plasma fills the region from $x = 0.05$ m to $x = 0.15$ m with a number density of n_{in} . We consider three different initial number densities: $n_{in} = 10^{16} \text{ m}^{-3}$ for low density, $n_{in} = 10^{18} \text{ m}^{-3}$ for medium density, and $n_{in} = 10^{20} \text{ m}^{-3}$ for high density plasma. Both electrons and ions follow Maxwell distributions initially, with equal temperatures $T_i = T_e = 10$ eV, focusing on carbon ions ($m_i = 12$ atom). The initial electromagnetic field is set to 0, and a transverse electromagnetic wave is introduced at $x = 0$ with an electric field given by $E_{y,in}(t) = -E_{in}[1 + (t/t_{in})^4]^{-6} + E_{in}$, where the amplitude of the incident electric field is $E_{in} = -1.8 \times 10^8$ V/m and the response time is $t_{in} = 10^{-8}$ s.

In our simulation, we adopt the following reference values for length, temperature, number density, and mass: $x_0 = L$, $T_0 = T_e$, $n_0 = n_{in}$, $m_0 = m_e$. Following the dimensionless process described in section 2.1, we determine the reference values as follows: a reference magnetic field of $B_0 = 3.8 \times 10^{-5}$ T, a reference electric field of $E_0 = 50$ V, and a reference time of $t_0 = 1.5 \times 10^{-7}$ s. Consequently, the speed of light is $c = 226$ and the normalized Debye lengths λ for low, medium, and high density plasmas are 1.2×10^{-3} , 1.2×10^{-4} , and 1.2×10^{-5} , respectively. The dimensionless physics domain is $[0, 1]$, which is discretized with a grid size of $N_x = 100$. The electron velocity space spans $[-20, 5] \times [-5, 120]$, and the ion velocity space spans $[-5, 5] \times [-5, 5]$. Both the electron and ion velocity grids have a size of $N_{vx} \times N_{vy} = 100 \times 100$. The numerical time step is determined as $\Delta t = C\Delta x/v_{max}$, where $v_{max} = 120$ and $C = 0.9$. In this simulation, we set θ to 1. The physics boundary and electromagnetic field boundary of the distribution function are implemented using zero-inflow boundary [8] and the absorption boundary [64]. Here the time scale and spatial scale are specifically defined with respect to electron oscillation period and electron Debye length, respectively, which are both represented by λ .

First, we consider the low-density plasma case with $\lambda = 1.2 \times 10^{-3}$. The numerical parameters for this case are $\Delta x = 10^{-2} = 8.5\lambda$ and $\Delta t = 7.5 \times 10^{-5} = 6.4 \times 10^{-2}\lambda$, indicating that the spatial resolution is lower than the electron Debye length, but the time resolution is sufficient. Fig. 5 illustrates the spatial distributions of the low-density POS plasma and the electromagnetic field. The results from the CSL-RME agree well with those obtained from the CSL-ME. Despite the fact that the physics grid does not well resolve electron Debye length, CSL-ME still yields a stable numerical solution. This is due to the fact that the time step employed in the simulation already resolves the electron oscillation period [27]. It is noteworthy that the CSL-RME with $N_x = 100$ produces results comparable to those obtained from the AP-PIC [3] with $N_x = 1000$, but without numerical noise. In Fig. 5 (a), we can observe that due to the significantly smaller mass of electrons compared to ions, electrons are more easily accelerated by electromagnetic waves, as depicted in Fig. 5 (b). Consequently, they escape from the main plasma, leading to disruption of the quasi-neutral region and the formation of a sheath. This charge separation induces a strong electric field E_x , as shown in Fig. 5 (c). Simultaneously, the magnetic field efficiently penetrates through the plasma, as illustrated in Fig. 5 (d). In this simulation, the PP limiter is crucial to prevent the occurrence of negative electron number densities and numerical oscillations.

Then, we consider the medium-density plasma with $\lambda = 1.2 \times 10^{-4}$. The numerical parameters for this case are $\Delta x = 85\lambda$ and $\Delta t = 0.64\lambda$. Remarkably, as shown in Fig. 6, the CSL-RME solution remains in good agreement with CSL-ME, even with a larger

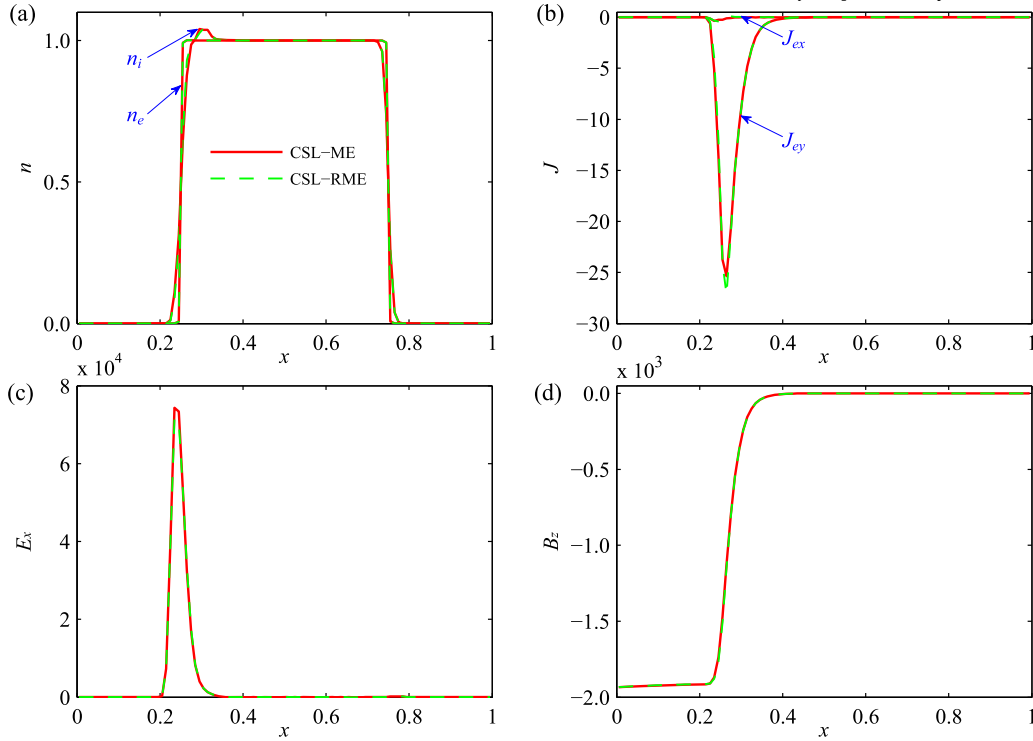


Fig. 6. POS: $\lambda = 1.2 \times 10^{-4}$. The plasma density n (a), current density J (b), electric field E_x (c) and magnetic field B_z (d) against physics space x at $t = 0.026$.

value of $\Delta x = 85\lambda$. A comparison between the medium-density case and the previous low-density case shown in Fig. 5 reveals several notable differences. Firstly, the width of plasma sheath is narrower in the medium-density case, as depicted in Fig. 6 (a). Moreover, the electric field E_x is stronger, as shown in Fig. 6 (c). Additionally, the generated current density by plasma is higher, as observed in Fig. 6 (b) (note that the reference density differs between the cases). Consequently, the magnetic field is effectively confined and prevented from penetrating into the main plasma, as illustrated in Fig. 6 (d). However, within the non-neutral region ($0.25 < x < 0.35$), a strong magnetic field B_z is generated. These findings highlight the influence of plasma density on the characteristics of the plasma sheath and the associated electromagnetic fields.

In the high-density plasma case, the numerical parameters are $\Delta x = 850\lambda$ and $\Delta t = 6.4\lambda$, CSL-ME fails to provide a stable numerical solution due to insufficient resolution of the oscillation period. Encouragingly, CSL-RME still provides a stable and satisfactory solution, as depicted in Fig. 7. Notably, the main plasma region in the high-density case exhibits a predominantly quasi-neutral behavior, as shown in Fig. 7 (a). This can be attributed to the significant electron current density observed in Fig. 7 (b), the incident electric field depicted in Fig. 7 (c), and the magnetic field shown in Fig. 7 (d). These quantities experience significant reflection at the plasma edge, consistent with previous research [3]. These simulations demonstrate the advantageous AP properties of CSL-RME, which enable the effective handling of high-density plasmas and the transition from vacuum to high density plasma, even with coarse discretizations.

The above arguments indicate that, when the plasma oscillation period is not resolved, CSL-ME fails to provide stable results, while CSL-RME still can provide the reasonable results, exhibiting favorable AP properties in the quasi-neutral limit. Additionally, it is important to note that the computational cost of CSL-RME is comparable to that of CSL-ME per time step. This implies that CSL-RME offers a competitive computational efficiency, making it a viable choice for simulations while maintaining accuracy and stability.

5.4. Magnetic reconnection

In this section, we apply the CSL-RME to a 2d3v magnetic reconnection simulation known as the Geospace Environmental Modelling (GEM) challenge. This simulation poses a significant numerical challenge due to its multidimensional nature, and it serves as a rigorous test for evaluating the accuracy, stability, and efficiency of the proposed CSL-RME method. The simulation involves the dynamics of both ions and electrons, following VM system, which has been previously described and will not be reiterated here.

Here, we utilize the GEM challenge proposed by Birn et al. [65], where the initial magnetic field in the $x - y$ plane is governed by the Harris equilibrium distribution,

$$\mathbf{B}(y) = B_0 \tanh(y/\lambda_0) \mathbf{e}_x, \tag{52}$$

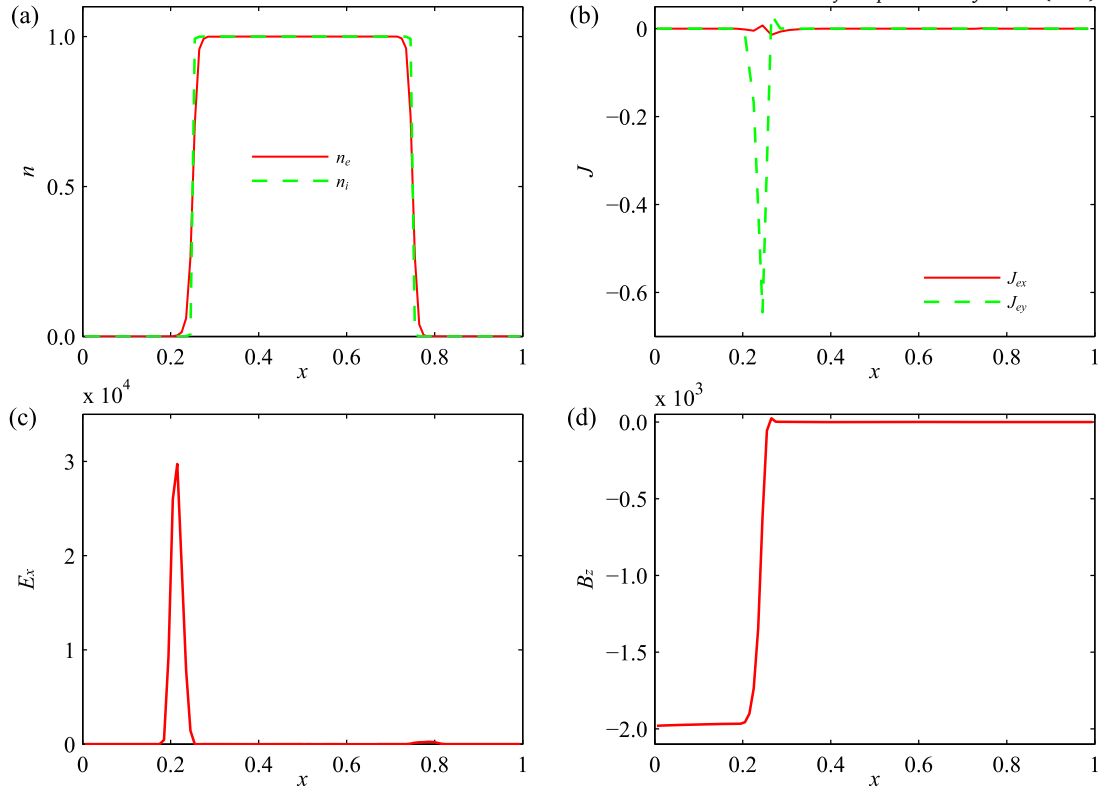


Fig. 7. POS: $\lambda = 1.2 \times 10^{-5}$. The plasma density n (a), current density J (b), electric field E_x (c) and magnetic field B_z (d) against physics space x at $t = 0.026$.

where $\lambda_0 = \lambda_i/2$ represents the half thickness of the current sheet, and $\lambda_i = c/\omega_{pi}$ corresponds to the ion inertial length. The initial electric fields are set to zero. The initial distribution of electrons and ions follows a shifted Maxwellian distribution,

$$f_s^0 = \frac{n(y)}{(\sqrt{2\pi}v_{ts})^3} \exp\left[-\frac{v_x^2 + v_y^2 + (v_z - v_{ds})^2}{2v_{ts}^2}\right], \quad (53)$$

where the initial plasma number density is given by $n(y) = n_0 \text{sech}^2(y/\lambda_0)$. Slightly different from the original GEM simulation, in this study, the x -coordinate is chosen as GSM- x , the y -coordinate is chosen as GSM- z , and the z -coordinate is chosen in the opposite direction of GSM- y .

To investigate the steady-state collisionless magnetic reconnection, we combine Eq. (52) with the Ampère's law without the time-varying electric field term, yielding,

$$\frac{B_0}{\lambda_0} \text{sech}^2(y/\lambda_0) = -\mu_0 q n_0 (v_{di} - v_{de}). \quad (54)$$

By substituting Eq. (53) and Eq. (54) into the Vlasov equation, we can easily obtain the drift velocity as follows,

$$v_{ds} = -\frac{2m_s v_{ts}^2}{q_s B_0 \lambda_0}. \quad (55)$$

Furthermore, considering the balance between plasma thermal energy and magnetic energy, we can obtain the plasma thermal velocity,

$$v_{ts} = \sqrt{\frac{\Theta_s B_0^2}{2\mu_0 n_s m_s}}, \quad (56)$$

where $\Theta_s = \frac{T_s}{T_e + T_i}$ is the temperature ratio coefficient. Similar to other kinetic magnetic reconnection simulations [16,33,34,66,67], we choose the ion-to-electron temperature ratio as $T_i/T_e = 5$, the reduced mass ratio as $m_i/m_e = 25$, and the Alfvén velocity as $v_a = c/20$. The physics computational domain is $[-L_x, L_x] \times [-L_y, L_y]$, where $L_x = 12.8\lambda_i$ and $L_y = 6.4\lambda_i$.

In our simulation, the reference length, mass, and number density are chosen as the ion inertial length λ_i , ion mass m_i , initial plasma number density n_0 , respectively. The reference temperature is chosen as $T_0 = m_i v_a^2/k_B$, which determines the reference velocity as

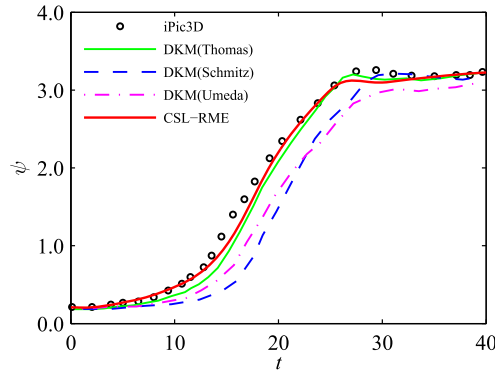


Fig. 8. Magnetic reconnection: $\Delta t = 0.02$. Time evolution of reconnected flux predicted by CSL-RME, compared to the results of iPic3D [66], DKM(Thomas) [67], DKM(Schmitz) [34], and DKM(Umeda) [33](b).

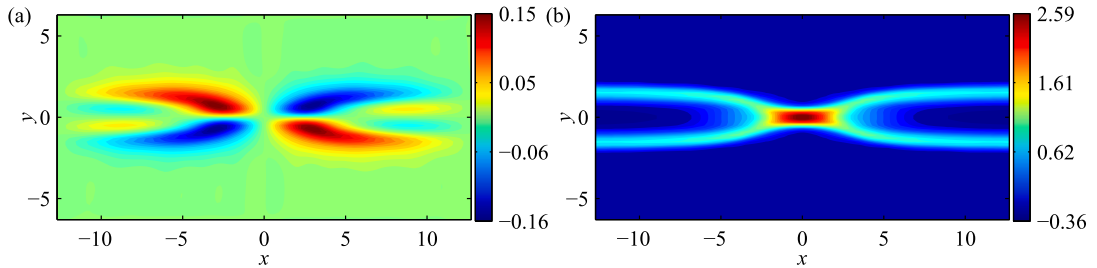


Fig. 9. Magnetic reconnection: The out-of-plane magnetic field B_z (a) and the electron velocity u_{ze} (b) at $t = 16$.

the Alfvén velocity v_a , and the reference time as the ion cyclotron period ω_{ci}^{-1} . According to the dimensionless process described in Section 2.1, we have the dimensionless speed of light $c = 20$, ion inertial length $\lambda_i = 1$, and initial magnetic field $B_0 = 1$. From Eq. (56), we obtain the ion thermal speed $v_{ti} = \sqrt{5/12}$ and the electron thermal speed $v_{te} = \sqrt{25/12}$, while from Eq. (55), we have the ion drift speed $v_{di} = -5/3$ and the electron drift speed $v_{de} = 1/3$. Correspondingly, plasma frequency $\omega_{pe} = 100$. The left and right boundaries are set as periodic boundaries, while the top and bottom boundaries are set as conducting walls. The physics space is discretized with a grid size of $N_x \times N_y$, where $N_x = 2N_y$. The electron velocity space is discretized in the range $[-8v_{te}, 8v_{te}]^3$, and the ion velocity space is discretized in the range $[-9v_{ti}, 9v_{ti}]^3$. Both velocity spaces adopt a uniform grid with $N_{v_x} \times N_{v_y} \times N_{v_z} = 26 \times 26 \times 26$. The time step is set as $\Delta t = 0.02$, the simulation time is up to $t = 40$, and the physics grid size is $N_x = 128$. Besides, a background particle with a density of $n_b = 0.2n_0$ is introduced in the simulation. To trigger magnetic reconnection, a small perturbed magnetic island is introduced into the equilibrium field, denoted as $\delta \mathbf{B} = \nabla \phi \times \mathbf{e}_z$, where $\phi(x, y) = \phi_0 \cos(\pi x/L_x) \cos(\pi y/2L_y)$, and $\phi_0 = 0.1B_0\lambda_i$. Additionally, small perturbed magnetic fields can be added near the diffusion region to accelerate the reconnection process [68].

The magnetic flux $\psi = \int_0^{L_x} B_y(x, y = 0) dx$ is an important parameter that is commonly used to validate numerical methods. Fig. 8 presents the time evolution of magnetic flux predicted by different kinetic methods, including the implicit PIC method iPic3D [66] and other DKM methods [16,33,34]. As shown in the figure, there are slight differences in the predicted magnetic flux evolution among different kinetic methods. The results obtained by proposed CSL-RME are in good agreement with those of iPic3D [67], with the magnetic flux reaching 1 around $t = 16$, slightly earlier than the predictions of Schmitz et al. [34] and Umeda et al. [33]. However, all the methods predict that the magnetic flux reaches a steady state at $t > 30$.

Previous research works [65,66] have shown that the difference in ion and electron dynamics leads to the generation of Hall currents, which in turn produce an out-of-plane magnetic field with a quadrupolar structure, which plays a crucial role in magnetic reconnection. Encouragingly, the proposed CSL-RME is able to reproduce the quadrupolar structure of the out-of-plane magnetic field B_z , as depicted in Fig. 9 (a). Additionally, Fig. 9 (b) displays the out-of-plane electron velocity u_{ze} , revealing a discernible central diffusion region with a width of approximately five ion inertial lengths [69].

Fig. 10 shows magnetic lines and the contours of the out-of-plane current density J_z . We focus on the time $t = 16$ onwards, corresponding to a reconnected flux $\psi = 1$ as shown in Fig. 8. At $t = 16$, the central region of current density initiates separation, indicating the presence of a separatrix in the magnetic topology, as shown in Fig. 10 (a). Subsequently, the current density undergoes rearrangement within the diffusion region, leading to a rapid reconnection process. At $t = 40$, the separatrix and X-point become prominent, as illustrated in Fig. 10 (b). It should be noted that in the current CSL-RME simulation, the grid spacing is approximately 14 times larger than the Debye length, and the time step is 2 times the electron oscillation period ω_{pe}^{-1} . Despite the unresolved electron oscillation period and the severe under-resolution of the Debye length, the CSL-RME method remains stable and produces qualitatively similar results to higher-resolution simulations published in [33,34].

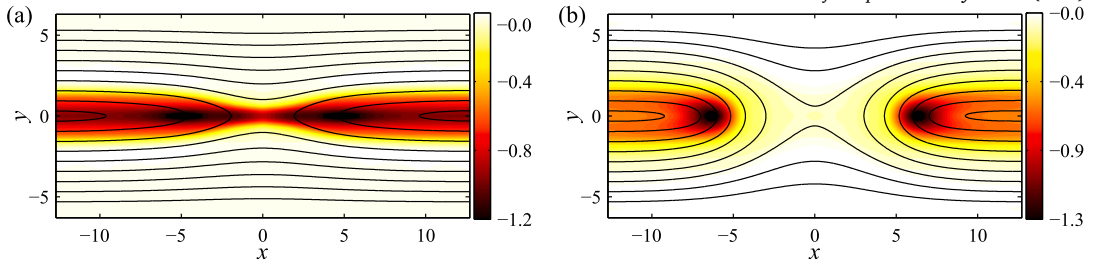


Fig. 10. Magnetic reconnection. Magnetic field lines (black solid line) and the contours of out-of-plane current density J_z at $t = 16$ (a) and $t = 40$ (b).

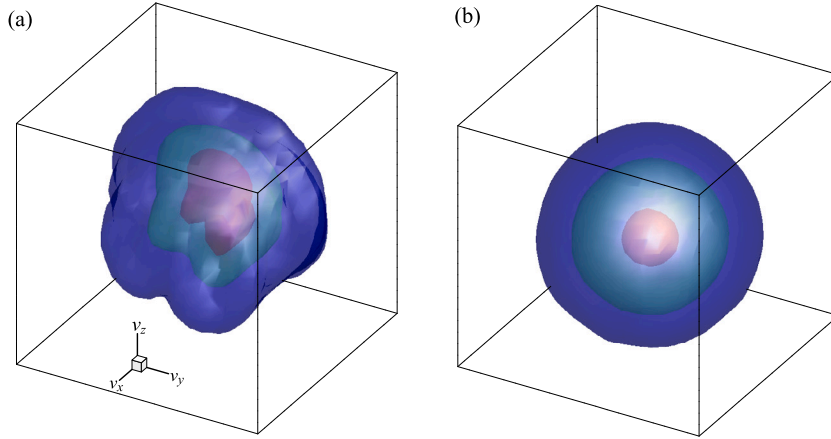


Fig. 11. Magnetic reconnection. Isosurfaces of electrons distribution function $f_e(v_x, v_y, v_z)$ for $x = 0, y = 0$ at $t = 16$ (a) and $t = 40$ (b). The velocity box ranges from $[-6.5v_{te}, 6.5v_{te}]$ for v_x and v_y and $[-5v_{te}, 8v_{te}]$ for v_z .

As a direct kinetic method, CSL-RME enables the easy acquisition of the velocity distribution function, facilitating a more comprehensive understanding of dynamic properties of particles in magnetic reconnection. Fig. 11 presents electrons distribution function at the magnetic null point ($x = 0, y = 0$). As shown in Fig. 11 (a), at $t = 16$, electrons distribution function exhibits significant anisotropy, indicating strong non-equilibrium features. This highlights the necessity of kinetic simulations in capturing the correct dynamic characteristics of particles in this region. With the rapid development of reconnection, as reconnection reaches a steady state, as shown in Fig. 11 (b) at $t = 40$, the electrons distribution exhibits an equilibrium state, exhibiting isotropy.

The above arguments indicate that the proposed CSL-RME maintains favorable accuracy and stability in challenging multidimensional simulations, even when the electron oscillation period is unresolved and the Debye length is severely under-resolved.

6. Conclusions

We have presented an asymptotic-preserving conservative Semi-Lagrangian (CSL) scheme for the Vlasov-Maxwell system. The key ingredients of the proposed method include the reformulated Maxwell equation obtained by semi-implicitly coupling of particle transport and electric field, as well as tracking of particle trajectories by using CSL scheme. These key ingredients allow the proposed method can provide reliable results in both quasi-neutral and non-quasi-neutral regimes even when the grid size and time step cannot resolve the Debye length and plasma period. Moreover, employing high-order CSL schemes ensures stable, accurate simulations that conserve system mass, even with very large CFL numbers. Importantly, the proposed method offers comparable computational complexity and cost per time step to explicit schemes, making it a promising alternative for plasma simulations, specially in multiscale simulations.

Continuing our research efforts to build upon the results presented above. When the computational time step cannot resolve the plasma oscillation period, the current method suppresses the rapid growth of the electric field and numerical heating. However, we acknowledge that, similar to semi-implicit particle methods [2,3], the current method can potentially introduce energy damping, which may lead to unphysical numerical cooling. In our near future work, we will develop an energy conserving kinetic scheme for electromagnetic plasma simulation. Additionally, as we progress towards conducting more realistic 3d3v simulations, the current method suffers from the curse of high dimensionality. We will actively investigate and implement memory reduction techniques to further enhance the computational efficiency of the proposed method.

CRediT authorship contribution statement

Hongtao Liu: Writing – original draft, Validation, Software, Methodology, Conceptualization. **Xiaofeng Cai:** Writing – review & editing, Validation, Methodology. **Yong Cao:** Validation, Funding acquisition. **Giovanni Lapenta:** Writing – review & editing, Supervision, Resources, Funding acquisition.

Declaration of competing interest

The authors declared that they have no conflicts of interest to this work. We declare that we do not have any commercial or associative interest that represents a conflict of interest in connection with the work submitted.

Acknowledgements

At KU Leuven, the work was supported by the KU Leuven Bijzonder Onder-zoeksfonds (BOF) under the C1 project TRACESpace and by the European Union's project DEEP-SEA (Grant agreement 955606). This work was supported by a PostDoctoral Fellowship 1252224N from Research Foundation-Flanders (FWO). Cai was partially supported by the National Natural Science Foundation (China) [Grant Number 12201052], the Guangdong Provincial Key Laboratory of Interdisciplinary Research and Application for Data Science, [2022B1212010006], National Key Laboratory for Computational Physics [6142A05230201]. Additionally, this work received partial support from Guangdong Basic and Applied Basic Research Foundation (No. 2023A1515010137) Shenzhen Technology Project (No. GJHZ20220913143010019).

Data availability

Data will be made available on request.

References

- [1] F.F. Chen, *Introduction to Plasma Physics and Controlled Fusion*, vol. 1, Springer, 1984.
- [2] S. Markidis, G. Lapenta, et al., Multi-scale simulations of plasma with iPIC3D, *Math. Comput. Simul.* 80 (2010) 1509–1519.
- [3] P. Degond, F. Deluzet, D. Doyen, Asymptotic-preserving particle-in-cell methods for the Vlasov–Maxwell system in the quasi-neutral limit, *J. Comput. Phys.* 330 (2017) 467–492.
- [4] C. Birdsall, A. Langdon, *Plasma Physics via Computer Simulation*, Taylor & Francis, 2004.
- [5] G. Lapenta, Particle simulations of space weather, *J. Comput. Phys.* 231 (2012) 795–821.
- [6] G. Lapenta, Exactly energy conserving semi-implicit particle in cell formulation, *J. Comput. Phys.* 334 (2017) 349–366.
- [7] E. Camporeale, G.L. Delzanno, B. Bergen, J.D. Moulton, On the velocity space discretization for the Vlasov–Poisson system: comparison between implicit Hermite spectral and Particle-in-Cell methods, *Comput. Phys. Commun.* 198 (2016) 47–58.
- [8] H. Liu, L. Quan, Q. Chen, S. Zhou, Y. Cao, Discrete unified gas kinetic scheme for electrostatic plasma and its comparison with the particle-in-cell method, *Phys. Rev. E* 101 (2020) 043307.
- [9] K. Xu, J.-C. Huang, A unified gas-kinetic scheme for continuum and rarefied flows, *J. Comput. Phys.* 229 (2010) 7747–7764.
- [10] Z. Guo, K. Xu, R. Wang, Discrete unified gas kinetic scheme for all Knudsen number flows: low-speed isothermal case, *Phys. Rev. E* 88 (2013) 033305.
- [11] H. Liu, Y. Cao, Q. Chen, M. Kong, L. Zheng, A conserved discrete unified gas kinetic scheme for microchannel gas flows in all flow regimes, *Comput. Fluids* 167 (2018) 313–323.
- [12] H. Liu, M. Kong, Q. Chen, L. Zheng, Y. Cao, Coupled discrete unified gas kinetic scheme for the thermal compressible flows in all Knudsen number regimes, *Phys. Rev. E* 98 (2018) 053310.
- [13] J. Chen, S. Liu, Y. Wang, C. Zhong, Conserved discrete unified gas-kinetic scheme with unstructured discrete velocity space, *Phys. Rev. E* 100 (2019) 043305.
- [14] T. Chen, X. Wen, L.-P. Wang, Z. Guo, J. Wang, S. Chen, Simulation of three-dimensional compressible decaying isotropic turbulence using a redesigned discrete unified gas kinetic scheme, *Phys. Fluids* 32 (2020) 125104.
- [15] L. Yang, X. Zhao, C. Shu, Y. Du, Parametric reduced order modeling-based discrete velocity method for simulation of steady rarefied flows, *J. Comput. Phys.* (2020) 110037.
- [16] H. Liu, X. Cai, G. Lapenta, Y. Cao, Conservative semi-Lagrangian kinetic scheme coupled with implicit finite element field solver for multidimensional Vlasov Maxwell system, *Commun. Nonlinear Sci. Numer. Simul.* 102 (2021) 105941.
- [17] H. Liu, M. Chen, X. Cai, Y. Cao, G. Lapenta, A combined immersed finite element and conservative semi-Lagrangian scheme for plasma-material interactions, *J. Comput. Phys.* 488 (2023) 112232.
- [18] T. Xiong, J.-M. Qiu, Z. Xu, A. Christlieb, High order maximum principle preserving semi-Lagrangian finite difference WENO schemes for the Vlasov equation, *J. Comput. Phys.* 273 (2014) 618–639.
- [19] S.Y. Cho, S. Boscarino, G. Russo, S.-B. Yun, Conservative semi-Lagrangian schemes for kinetic equations part II: applications, *J. Comput. Phys.* (2021) 110281.
- [20] J.-M. Qiu, A. Christlieb, A conservative high order semi-Lagrangian WENO method for the Vlasov equation, *J. Comput. Phys.* 229 (2010) 1130–1149.
- [21] R.E. Heath, I.M. Gamba, P.J. Morrison, C. Michler, A discontinuous Galerkin method for the Vlasov–Poisson system, *J. Comput. Phys.* 231 (2012) 1140–1174.
- [22] J.A. Rossmannith, D.C. Seal, A positivity-preserving high-order semi-Lagrangian discontinuous Galerkin scheme for the Vlasov–Poisson equations, *J. Comput. Phys.* 230 (2011) 6203–6232.
- [23] J.-M. Qiu, C.-W. Shu, Positivity preserving semi-Lagrangian discontinuous Galerkin formulation: theoretical analysis and application to the Vlasov–Poisson system, *J. Comput. Phys.* 230 (2011) 8386–8409.
- [24] F. Filbet, E. Sonnendrücker, P. Bertrand, Conservative numerical schemes for the Vlasov equation, *J. Comput. Phys.* 172 (2001) 166–187.
- [25] J.W. Banks, J.A.F. Hittinger, A new class of nonlinear finite-volume methods for Vlasov simulation, *IEEE Trans. Plasma Sci.* 38 (2010) 2198–2207.
- [26] C. Liu, K. Xu, A unified gas kinetic scheme for continuum and rarefied flows V: multiscale and multi-component plasma transport, *Commun. Comput. Phys.* 22 (2017) 1175–1223.
- [27] H. Liu, F. Shi, J. Wan, X. He, Y. Cao, Discrete unified gas kinetic scheme for a reformulated BGK–Vlasov–Poisson system in all electrostatic plasma regimes, *Comput. Phys. Commun.* (2020) 107400.

- [28] S. Le Bourdieu, F. De Vuyst, L. Jacquet, Numerical solution of the Vlasov–Poisson system using generalized Hermite functions, *Comput. Phys. Commun.* 175 (2006) 528–544.
- [29] T. Arber, R. Vann, A critical comparison of Eulerian-grid-based Vlasov solvers, *J. Comput. Phys.* 180 (2002) 339–357.
- [30] F. Filbet, E. Sonnendrücker, Comparison of Eulerian Vlasov solvers, *Comput. Phys. Commun.* 150 (2003) 247–266.
- [31] G. Dimarco, L. Pareschi, Numerical methods for kinetic equations, *Acta Numer.* (2014) 369–520.
- [32] L. Einkemmer, A performance comparison of semi-Lagrangian discontinuous Galerkin and spline based Vlasov solvers in four dimensions, *J. Comput. Phys.* 376 (2019) 937–951.
- [33] T. Umeda, K. Togano, T. Ogino, Two-dimensional full-electromagnetic Vlasov code with conservative scheme and its application to magnetic reconnection, *Comput. Phys. Commun.* 180 (2009) 365–374.
- [34] H. Schmitz, R. Grauer, Kinetic Vlasov simulations of collisionless magnetic reconnection, *Phys. Plasmas* 13 (2006) 092309.
- [35] K. Kormann, K. Reuter, M. Rampp, A massively parallel semi-Lagrangian solver for the six-dimensional Vlasov–Poisson equation, *Int. J. High Perform. Comput. Appl.* 33 (2019) 924–947.
- [36] X. Cai, W. Guo, J.-M. Qiu, A high order semi-Lagrangian discontinuous Galerkin method for Vlasov–Poisson simulations without operator splitting, *J. Comput. Phys.* 354 (2018) 529–551.
- [37] H. Liu, X. Cai, Y. Cao, G. Lapenta, An efficient energy conserving semi-Lagrangian kinetic scheme for the Vlasov–Ampère system, *J. Comput. Phys.* (2023) 112412.
- [38] A. Crestetto, N. Crouseilles, M. Lemou, Kinetic/fluid micro-macro numerical schemes for Vlasov–Poisson–BGK equation using particles, *Kinet. Relat. Models* 5 (2012) 787–816.
- [39] G. Dimarco, L. Pareschi, Fluid solver independent hybrid methods for multiscale kinetic equations, *SIAM J. Sci. Comput.* 32 (2010) 603–634.
- [40] S. Jin, Efficient asymptotic-preserving (AP) schemes for some multiscale kinetic equations, *SIAM J. Sci. Comput.* 21 (1999) 441–454.
- [41] F. Filbet, S. Jin, A class of asymptotic-preserving schemes for kinetic equations and related problems with stiff sources, *J. Comput. Phys.* 229 (2010) 7625–7648.
- [42] R. Belaouar, N. Crouseilles, P. Degond, E. Sonnendrücker, An asymptotically stable semi-Lagrangian scheme in the quasi-neutral limit, *J. Sci. Comput.* 41 (2009) 341–365.
- [43] P. Degond, F. Deluzet, L. Navoret, A.-B. Sun, M.-H. Vignal, Asymptotic-preserving particle-in-cell method for the Vlasov–Poisson system near quasineutrality, *J. Comput. Phys.* 229 (2010) 5630–5652.
- [44] P. Degond, F. Deluzet, L. Navoret, An asymptotically stable particle-in-cell (pic) scheme for collisionless plasma simulations near quasineutrality, *C. R. Acad. Sci. Paris Ser.* 343 (2006) 613–618.
- [45] G. Manfredi, S. Hirstoaga, S. Devaux, Vlasov modelling of parallel transport in a tokamak scrape-off layer, *Plasma Phys. Control. Fusion* 53 (2010) 015012.
- [46] N. Crouseilles, G. Dimarco, M.-H. Vignal, Multiscale schemes for the BGK–Vlasov–Poisson system in the quasi-neutral and fluid limits. Stability analysis and first order schemes, *Multiscale Model. Simul.* 14 (2016) 65–95.
- [47] L. Ji, Z. Yang, Z. Li, D. Wu, S. Jin, Z. Xu, An asymptotic-preserving and energy-conserving particle-in-cell method for Vlasov–Maxwell equations, *J. Math. Phys.* 64 (2023).
- [48] C.-D. Munz, P. Omnes, R. Schneider, E. Sonnendrücker, U. Voss, Divergence correction techniques for Maxwell solvers based on a hyperbolic model, *J. Comput. Phys.* 161 (2000) 484–511.
- [49] M.C. Pinto, M. Mounier, E. Sonnendrücker, Handling the divergence constraints in Maxwell and Vlasov–Maxwell simulations, *Appl. Math. Comput.* 272 (2016) 403–419.
- [50] L. Einkemmer, A. Ostermann, C. Piazzola, A low-rank projector-splitting integrator for the Vlasov–Maxwell equations with divergence correction, *J. Comput. Phys.* 403 (2020) 109063.
- [51] J.P. Boris, et al., Relativistic plasma simulation-optimization of a hybrid code, in: *Proc. Fourth Conf. Num. Sim. Plasmas*, 1970, pp. 3–67.
- [52] U.S. Inan, M. Gołkowski, *Principles of Plasma Physics for Engineers and Scientists*, Cambridge University Press, 2010.
- [53] H. Schmitz, R. Grauer, Comparison of time splitting and backsubstitution methods for integrating Vlasov’s equation with magnetic fields, *Comput. Phys. Commun.* 175 (2006) 86–92.
- [54] N. Crouseilles, L. Einkemmer, E. Faou, Hamiltonian splitting for the Vlasov–Maxwell equations, *J. Comput. Phys.* 283 (2015) 224–240.
- [55] Y. Cao, X. He, T. Lü, A splitting extrapolation for solving nonlinear elliptic equations with d-quadratic finite elements, *J. Comput. Phys.* 228 (2009) 109–122.
- [56] G. Chen, L. Chacón, C.A. Leibs, D.A. Knoll, W. Taitano, Fluid preconditioning for Newton–Krylov-based, fully implicit, electrostatic particle-in-cell simulations, *J. Comput. Phys.* 258 (2014) 555–567.
- [57] S. Markidis, G. Lapenta, The energy conserving particle-in-cell method, *J. Comput. Phys.* 230 (2011) 7037–7052.
- [58] A.B. Langdon, B.I. Cohen, A. Friedman, Direct implicit large time-step particle simulation of plasmas, *J. Comput. Phys.* 51 (1983) 107–138.
- [59] J. Bai, Y. Cao, X. He, E. Peng, An implicit particle-in-cell model based on anisotropic immersed-finite-element method, *Comput. Phys. Commun.* 261 (2021) 107655.
- [60] Y. Cheng, I.M. Gamba, F. Li, P.J. Morrison, Discontinuous Galerkin methods for the Vlasov–Maxwell equations, *SIAM J. Numer. Anal.* 52 (2014) 1017–1049.
- [61] M. Kraus, K. Kormann, P.J. Morrison, E. Sonnendrücker, Gempic: geometric electromagnetic particle-in-cell methods, *J. Plasma Phys.* 83 (2017).
- [62] L. Palodhi, F. Califano, F. Pegoraro, Nonlinear kinetic development of the Weibel instability and the generation of electrostatic coherent structures, *Plasma Phys. Control. Fusion* 51 (2009) 125006.
- [63] Y. Cheng, A.J. Christlieb, X. Zhong, Energy-conserving discontinuous Galerkin methods for the Vlasov–Maxwell system, *J. Comput. Phys.* 279 (2014) 145–173.
- [64] F. Deluzet, Mathematical modeling of plasma opening switches, *Comput. Phys. Commun.* 152 (2003) 34–54.
- [65] J. Birn, J. Drake, M. Shay, B. Rogers, R. Denton, M. Hesse, M. Kuznetsova, Z. Ma, A. Bhattacharjee, A. Otto, et al., Geospace environmental modeling (GEM) magnetic reconnection challenge, *J. Geophys. Res.* 106 (2001) 3715–3719.
- [66] P. Ricci, G. Lapenta, J. Brackbill, A simplified implicit Maxwell solver, *J. Comput. Phys.* 183 (2002) 117–141.
- [67] T.A. Trost, Coupling of Vlasov- and fluid-codes with adaptive domain decomposition using the example of magnetic reconnection, Ph.D. thesis, Ruhr-Universität Bochum, 2017.
- [68] G. Lapenta, S. Markidis, A. Divin, M. Goldman, D. Newman, Scales of guide field reconnection at the hydrogen mass ratio, *Phys. Plasmas* 17 (2010) 082106.
- [69] P. Ricci, G. Lapenta, J. Brackbill, Gem reconnection challenge: implicit kinetic simulations with the physical mass ratio, *Geophys. Res. Lett.* 29 (2002) 3.